Available online at www.sciencedirect.com

SCIENCE DIRECT®

Polymer 45 (2004) 487–506

polymer

www.elsevier.com/locate/polymer

Multiscale micromechanical modeling of polymer/clay nanocomposites and the effective clay particle

N. Sheng[a], M.C. Boyce[a,*], D.M. Parks[a], G.C. Rutledge[b], J.I. Abes[b], R.E. Cohen[b]

[a]Department of Mechanical Engineering, Massachusetts Institute of Technology, 77 Massachusetts Avenue, Cambridge, MA 02139, USA
[b]Department of Chemical Engineering, Massachusetts Institute of Technology, Cambridge, MA 02139, USA

Received 31 May 2003; received in revised form 27 October 2003; accepted 30 October 2003

Abstract

Polymer/clay nanocomposites have been observed to exhibit enhanced mechanical properties at low weight fractions (W_c) of clay. Continuum-based composite modeling reveals that the enhanced properties are strongly dependent on particular features of the second-phase 'particles'; in particular, the particle volume fraction (f_p), the particle aspect ratio (L/t), and the ratio of particle mechanical properties to those of the matrix. These important aspects of as-processed nanoclay composites require consistent and accurate definition. A multiscale modeling strategy is employed to account for the hierarchical morphology of the nanocomposite: at a lengthscale of thousands of microns, the structure is one of high aspect ratio particles within a matrix; at the lengthscale of microns, the clay particle structure is either (a) exfoliated clay sheets of nanometer level thickness or (b) stacks of parallel clay sheets separated from one another by interlayer galleries of nanometer level height, and the matrix, if semi-crystalline, consists of fine lamella, oriented with respect to the polymer/nanoclay interfaces. Here, quantitative structural parameters extracted from XRD patterns and TEM micrographs (the number of silicate sheets in a clay stack, N, and the silicate sheet layer spacing, $d_{(001)}$) are used to determine geometric features of the as-processed clay 'particles', including L/t and the ratio of f_p to W_c. These geometric features, together with estimates of silica lamina stiffness obtained from molecular dynamics simulations, provide a basis for modeling effective mechanical properties of the clay particle. In the case of the semi-crystalline matrices (e.g. nylon 6), the transcrystallization behavior induced by the nanoclay is taken into account by modeling a layer of matrix surrounding the particle to be highly textured and therefore mechanically anisotropic. Micromechanical models (numerical as well as analytical) based on the 'effective clay particle' were employed to calculate the overall elastic modulus of the amorphous and semi-crystalline polymer–clay nanocomposites and to compute their dependence on the matrix and clay properties as well as internal clay structural parameters. The proposed modeling technique captures the strong modulus enhancements observed in elastomer/clay nanocomposites as compared with the moderate enhancements observed in glassy and semi-crystalline polymer/clay nanocomposites. For the case where the matrix is semi-crystalline, the proposed approach captures the effect of transcrystallized matrix layers in terms of composite modulus enhancement, however, this effect is found to be surprisingly minor in comparison with the 'composite'-level effects of stiff particles in a matrix. The elastic moduli for MXD6-clay and nylon 6-clay nanocomposites predicted by the micromechanical models are in excellent agreement with experimental data. When the nanocomposite experiences a morphological transition from intercalated to completely exfoliated, only a moderate increase in the overall composite modulus, as opposed to the expected abrupt jump, was predicted.

Keywords: Polymer/clay nanocomposites; Nanoclay; Micromechanical modeling

1. Introduction

Polymeric materials are often reinforced by stiff fillers to improve mechanical properties. The efficiency of reinforcement depends on the filler aspect ratio, the filler mechanical properties, and the adhesion between the matrix and the filler. Single clay layers were proposed to be an ideal reinforcing agent in 1974 [1] due to their extremely high aspect ratio and also due to the nanometer filler thickness being comparable to the scale of the polymer chain structure. Two decades later, the Toyota research group (Kojima, Usuki, Kawasumi, Okada, Fukushima, Kurauchi, and Kamigaito, 1993) [2,3] revealed a major breakthrough in polymer/clay nanocomposite technology with the success of in situ polymerization of nylon 6/clay nanocomposites, a

---

* Corresponding author. Tel.: +1-617-253-2342; fax: +1-617-258-8742.
E-mail address: mcboyce@mit.edu (M.C. Boyce).

0032-3861/$ - see front matter © 2003 Published by Elsevier Ltd.
doi:10.1016/j.polymer.2003.10.100

synthesis method economically suitable for industrial production. A doubling of both the tensile modulus and strength was achieved with as little as 4.7-weight percent clay; furthermore, the property enhancements extend to relatively high temperatures and, indeed, act to substantially increase ‘transition temperatures’ over that of the parent homopolymer (an increase of 80 °C in the heat distortion temperature has been observed [2,3]). Over the last decade, polymer/clay nanocomposites have been observed to exhibit dramatic enhancement in many other physical properties, including barrier [4–6], flammability resistance [7], and ablation performance [8]. The nanocomposite technology has also been extended to various polymer systems, including elastomers [9,10] and epoxies [11,12]; different levels of property enhancement are achieved, depending on the chosen matrix polymer.

Mechanics-based composite models have proved successful in predicting the enhanced mechanical properties of conventional polymer/fiber and flake composites, where the filler lengthscale is on the order of tens of microns or larger. The continuum mechanics-based composite models generally include parameters such as the particle volume fraction, particle aspect ratio and orientation, and particle/matrix property ratios. Researchers have recently begun applying some of these models to assess the thermal-mechanical properties of polymer nanocomposites [13–16]. Concepts such as ‘matrix’ and ‘particle’, which are well-defined in conventional two-phase composites, can no longer be directly applied to polymer/clay nanocomposites due to the hierarchical nanometer lengthscale morphology of the particle structure and surrounding matrix, as recently emphasized by Brune and Bicerano [15]. Issues as basic as the proper description of the mechanical behavior of nanoparticles of atomic level thickness, as well as the proper conversion of filler weight fraction to particle volume fraction, require careful treatment if one is to understand the dependence of composite properties on nanoclay content and structure. In addition, the transcrystallization behavior of semi-crystalline matrix, induced by the presence of nanoclay, needs to be properly accounted for in order to achieve a comprehensive understanding of semi-crystalline polymer–clay nanocomposites.

In this paper, mechanics-based model predictions of the dependence of composite material stiffness on plate-like filler content are presented. The hierarchical nature of the underlying structure of polymer/nanoclay composites is then detailed, and the applicability of well-established models to this new class of composite material is discussed. A multiscale modeling strategy accounts for the hierarchical morphology of the nanocomposite through use of an ‘effective particle’, defined and employed to represent the inherently discrete nanoclay structure as a basic object in micromechanical modeling. Particular attention is given to the mechanical description of the clay sheets and incorporation of this description into an effective particle model. The potential for describing macroscopic mechanical property enhancements in terms of composite-level effects is explored, treating the nanocomposite as an appropriately described matrix containing a suitable dispersion of the ‘effective particles’. Model predictions of macroscopic modulus are in excellent agreement with experimental data for various polymer (amorphous vs. semi-crystalline)-clay nanocomposites.

2. Conventional ‘particle’-based micromechanical models

Prediction of the mechanical properties of discontinuous fiber/flake composite materials has been a subject of extensive study. The composite of interest is considered to consist of two homogeneous phases: matrix and high-aspect-ratio particles. Here, both analytical and numerical predictions of the overall composite stiffness are presented; stiffness enhancement mechanisms are then explored using simple, idealized shear-lag analysis and numerical solutions. These models can be readily applied to polymer/clay nanocomposites, where the intercalated nanoclay is a heterogeneous laminate-like structure (Section 3), with reasonable homogenization of the ‘effective particle’ geometry and properties (Section 4). Various material and geometrical models of intercalated particles are explored (Section 5). Finally, model results are favorably compared with a wide range of experimental data (Section 6).

2.1. Analytical micromechanical models

Numerous micromechanical models (e g. [17–25]) have been proposed to predict the elastic constants of discontinuous fiber/flake composites. These models generally depend on parameters including particle/matrix stiffness ratio E_p/E_m, particle volume fraction f_p, particle aspect ratio L/t, and orientation. In applications relevant to the present study, the particles and the matrix are assumed to be linearly elastic, either of which can be taken as isotropic or transversely isotropic. Here, E_p and E_m denote the elastic moduli of the particle and the matrix, respectively. Tucker [26] provides a good review of the application of several classes of micromechanical models to discontinuous fiber-reinforced polymers. He notes that, of the existing models, the widely used Halpin–Tsai equations [21–23] give reasonable estimates for effective stiffness, but the Mori–Tanaka type models [20,27] give the best results for large-aspect-ratio fillers. Here, we focus on prediction of the longitudinal stiffness, E_{11}, for composites filled with unidirectional disk-like particles. The Halpin–Tsai equation and a closed-form solution based on the Mori–Tanaka model [27] are given in Eqs. (1) and (2), respectively

$$\frac{E_{11}^{(\mathrm{H-T})}}{E_m} = \frac{1 + 2(L/t) f_p \eta}{1 - f_p \eta} \tag{1}$$

$$\eta = \frac{(E_p/E_m) - 1}{(E_p/E_m) + 2(L/t)},$$

$$\frac{E_{11}^{(M-T)}}{E_m} = \frac{1}{1 - f_p\zeta}, \qquad (2)$$

$$\zeta = [-2\nu_m A_3 + (1 - \nu_m)A_4 + (1 + \nu_m)A_5 A]/(-2A)$$

where f_p is particle volume fraction, ζ is a positive coefficient depending on the matrix Poisson ratio, ν_m, and constants A and A_i; A and A_i can be calculated from the matrix/particle properties and components of the Eshelby tensor [17], which depend on the particle aspect ratio (L/t) and dimensionless elastic constants of the matrix (see Ref. [27] for details).

Fig. 1 depicts the dependence of E_{11}/E_m on f_p, L/t, and E_p/E_m, as predicted by Eqs. (1) and (2) for aligned disk-shaped particles. Both models show the same expected trends, but the Halpin–Tsai model is consistently stiffer than the Mori–Tanaka model. By taking the Halpin–Tsai shape factor (given as $2L/t$ in Eq. (1)) to be an adjustable parameter, the Halpin–Tsai equations can give nearly identical results to the Mori–Tanaka model [14].

In Fig. 1(a), the predicted E_{11} increases almost linearly with increasing f_p, for a fixed L/t and E_p/E_m. Note that this only holds when f_p is small (Fig. 1(a) is plotted for the range $0.0 < f_p < 0.10$); in fact, for $f_p \ll 1$, Eqs. (1) and (2) can both be linearized in the form

$$\frac{E_{11}}{E_m} = 1 + Bf_p, \qquad (3)$$

where B is a positive constant (assuming $E_p/E_m > 1$), depending on particle aspect ratio and particle/matrix elastic properties.

Particles with large L/t or high E_p/E_m prove more efficient in stiffness enhancement. However, the dependencies of E_{11}/E_m on L/t and E_p/E_m for a fixed f_p are rather nonlinear, as shown in Fig. 1(b) and (c). Reduced load transfer efficiency associated with large L/t or high E_p/E_m accounts for this nonlinearity, as shown later using shear lag analysis in Section 2.2.

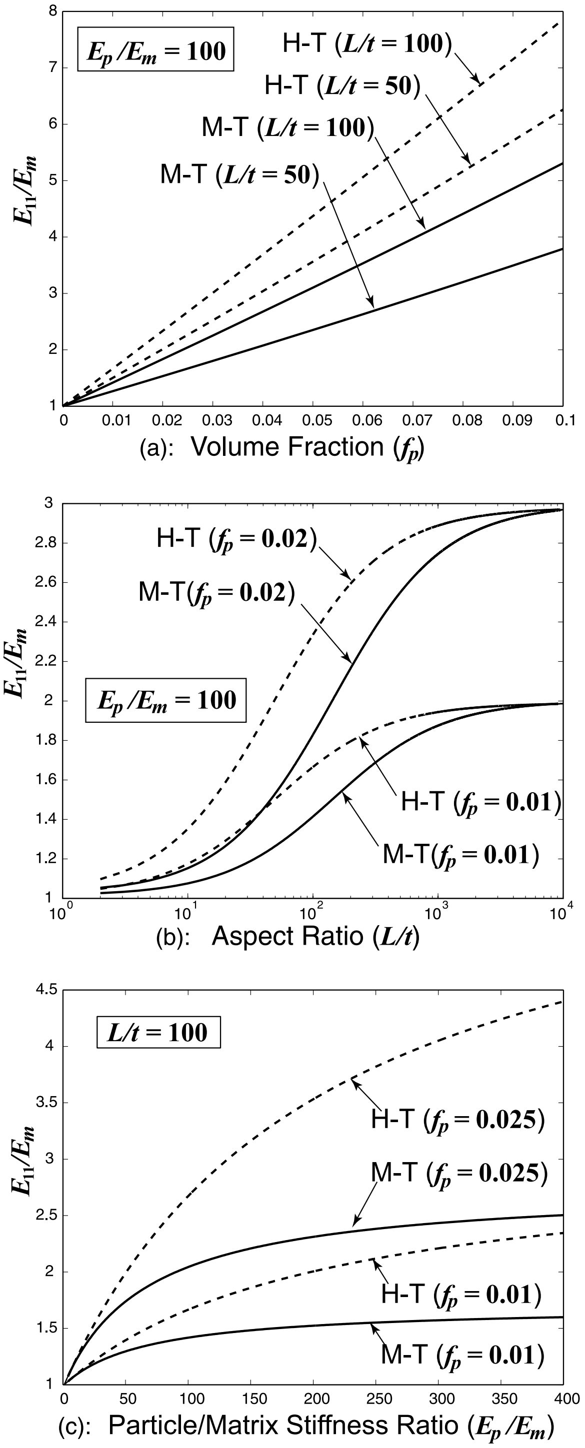

Fig. 1. Results of Mori–Tanaka model (M–T) and the Halpin–Tsai equations (H–T): dependence of E_{11} on (a) f_p, for $L/t = 50$ and 100, $E_p/E_m = 100$; (b) L/t, for $f_p = 0.01$ and 0.02, $E_p/E_m = 100$; (c) E_p/E_m, for $f_p = 0.01$ and 0.025, $L/t = 100$.

2.2. Numerical micromechanical model

2.2.1. Model description

Models of various representative volume elements (RVEs) of the underlying structure of the nano-clay filled polymers are constructed. The structure can be described by a set of geometric and material features. The geometric features of nano-clay filled polymer composites can be thought of in terms of features of clay particles; in particular, particle dispersion, particle volume fraction, particle aspect ratio, and particle orientation distribution. The material features can be described in terms of clay intercalation vs. exfoliation, clay/particle interface behavior, and polymer morphology (both in the vicinity of particles and away from particles). In this work, we focus our attention on the simplified case of uniform, well-aligned and *perfectly bonded* particles in an isotropic matrix, and examine the influence of the RVE representation of various geometric and constitutive features of the particles and their

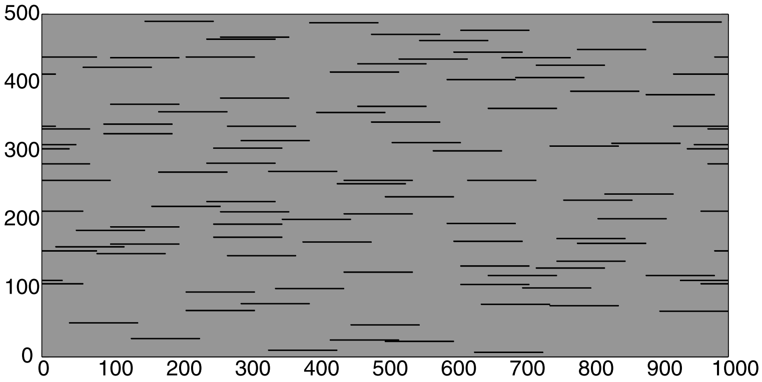

Fig. 2. A typical RVE for FEM micromechanical simulation ($f_p = 0.02$, $L/t = 100$, number of particles in the RVE = 100). Scales are in units of particle thickness, t.

distribution in the matrix. A typical RVE ($f_p = 0.02$, $L/t = 100/1$) used in the finite element method (FEM) based micromechanical modeling of this paper is shown in Fig. 2. The RVE dimensions are large compared to the characteristic size of the particle; the number of particles included in the RVE is large enough (~50–100) to obtain an accurate statistical representation of this structure. The structures are periodic in the direction of particle alignment; partial-length particles intersecting one lateral RVE boundary are completed by a remaining length, at the same elevation, intersecting the opposite lateral boundary.

Two-dimensional plane strain simulations of well-oriented random particle distributions are subject to small-strain axial tensile loading. Periodic boundary conditions expressed in terms of the macroscopic strain tensor ε are applied to the RVE. The macroscopic normal strain ε_{11} is used to drive the deformation of the entire RVE, which satisfies the kinematic periodic boundary conditions and equilibrium. Fig. 3 shows a schematic of (a) an undeformed RVE and RVEs subjected to (b) axial stretch in the x_1-direction while macroscopically traction free in the x_2-direction, and (c) simple shear. The exaggerated scale of deformation illustrates the periodic boundary conditions.[1]

The principle of virtual work has been used to calculate the overall mechanical response of the RVE, following Danielsson, Parks and Boyce [30]. Here, we adapt their scheme to the frame of small deformation gradients. Components of the macroscopic stress tensor σ are derived in terms of the generalized reaction forces of two 'auxiliary nodes', the 'displacement' components of which are those of the macroscopic strain tensor ε (see Ref. [30] for details).

All plane strain simulation results presented in this paper are normalized with corresponding plane strain properties of the isotropic matrix; for instance, the calculated plane strain longitudinal modulus, E^*_{11}, is normalized with respect to the matrix plane strain modulus E^*_m. For subsequent convenience, we do not further distinguish a plane strain property with ' $*$ ' in the remaining contents of this paper.

2.2.2. Results

The plane strain FEM simulation results of E_{11}/E_m are compared with the uniaxial analytical Mori–Tanaka model solution in Fig. 4(a), (b), and (c); the Mori–Tanaka-type model is chosen for comparison since it is among the more accurate analytical models [26]. Each FEM data point is averaged over numerical calculations of 10 random RVE realizations of a composite structure specified by f_p, L/t, and E_p/E_m; the variation in the macroscopic responses among these random realizations is reflected in Fig. 4 by error bars. The degree of variation tends to increase with increasing L/t or f_p; nevertheless, the averaged FEM results and the analytical model solutions exhibit similar trends. In particular, E_{11}/E_m is predicted to increase almost linearly with f_p by both FEM simulations and the Mori–Tanaka model (Fig. 4(a)), and the nonlinear dependencies of E_{11}/E_m on L/t (Fig. 4(b)) and on E_p/E_m (Fig. 4(c)) are captured by both numerical and analytical models as well. The underlying phenomenon governing these dependencies is the load transfer mechanism; i.e. the manner in which load is transmitted through the matrix to the particles.

When a discontinuous high-aspect-ratio particle composite is subjected to tensile loading, the load is transferred from the surrounding matrix to the particle mainly through interface shear stress. We speculate that this mechanism is also operative in nanoclay composites. Evidence supporting this proposition has been obtained in recent FTIR studies on nylon-6/nanoclay composites [31]. The clay FTIR peaks shift in a monotonic manner as the nanocomposite is subjected to increasing elastic strain, and reversibly shifts back upon unloading. These FTIR results document that strain and load are transmitted to the nanoclay sheets during loading of the composite [31].

First, we review the factors influencing load transfer efficiency using simple shear-lag concepts, which do not explicitly consider particle–particle interactions. Shear-lag analysis [24] reveals that large particle aspect ratio L/t and

---

[1] FEM-based micromechanical modeling of the mechanical behavior of materials containing random distributions of particles utilizing periodic boundary conditions have also been employed by other investigators (e.g. Bergström and Boyce [28]; Gusev [29]).

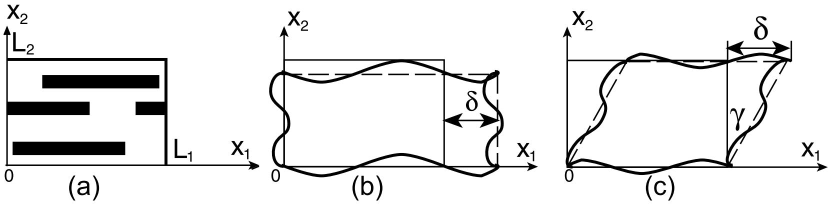

Fig. 3. Schematic of RVEs, illustrating periodic boundary conditions. (a) Undeformed RVE; (b) RVE under uniaxial tensile strain $\varepsilon_{11} = \delta/L_1$; (c) RVE under simple shear $\gamma_{12} = \delta/L_2$.

high relative matrix shear modulus G_m/E_p are desired for efficient stiffness reinforcement. Fig. 5(a) and (b) depict the effect of L/t and E_p/E_m on the particle axial strain distribution, ε_p, at a macroscopic axial strain $\varepsilon = 0.5\%$ (note that particle stress distributions are similar). Particles with larger L/t have higher maximum strain, ε_p^{max}, and longer effective length (the length of the central portion of the particle carrying significant load), L^e, as shown in Fig. 5(a); however, at sufficiently large L/t, $\varepsilon_p^{max} \rightarrow \varepsilon$, $L^e \rightarrow L$, and the average particle strain (stress) approaches a constant, leading to the saturation of E_{11}/E_m shown in Fig. 4(b). The saturation of E_{11}/E_m at high E_p/E_m (Fig. 4(c)) is a compromise result of two competing factors: the high filler stiffness tends to increase composite stiffness, but the low G_m/E_p ratio tends to reduce the load transfer efficiency. Decreases in both ε_p^{max} and L^e with increasing E_p/E_m (or decreasing G_m/E_p) are demonstrated in Fig. 5(b).

Fig. 6 shows the axial strain contour in a RVE loaded to $\varepsilon_{11} = 0.005$; the typical axial stress build-up in a particular 'isolated' particle is depicted in Fig. 6(a). The stress distributions in particles partly or completely 'overlapped' by other particles, as shown in Fig. 6(b) and (c), demonstrate the negative effects of particle interaction on load transfer efficiency: high-aspect-ratio particles shield the matrix from straining, and thus reduce the efficiency of load transfer to neighboring particles. As f_p or L/t increases, the chances of such deleterious particle interactions increase, which, in turn, leads to the nonlinear dependence of E_{11}/E_m on L/t, as shown in Fig. 4(b)[2]. The broadening of error bars with increasing f_p or L/t, shown in Fig. 4(a) and (b), can also be attributed to the increased extent of particle interaction; for a given f_p, particles with larger L/t have a higher tendency to cluster during a computer-generated 'random' seeding process, which will result in a significantly lower macroscopic E_{11} when the clustering is dominated by the kind of particle 'overlapping' shown in Fig. 6(c), but a higher E_{11} if the clustered particles form some inter-connected 'channels' due to close end-to-end distance rather than 'overlapping' of each other.

3. Hierarchical morphology of polymer/clay nanocomposites

The morphology of polymer/layered-silicate composites has a hierarchical structure. The dispersion of the clay in the matrix is typically described in terms of *intercalation* vs. *exfoliation*. In the *intercalated* structure, inter-layer domains of the primary clay particles are penetrated by polymer chains and consequently expand, with a typical inter-layer spacing of the order of 1–4 nm; in contrast, the *fully exfoliated* morphology consists of single silicate layers dispersed in a polymer matrix. In practice, however, many systems fall between these two idealized morphologies. Fig. 7 shows a TEM image of a nanocomposite containing both exfoliated and intercalated structures [32]. Different synthesis and processing histories will produce positional and orientational correlations between the platelets. These histories contribute to the development of a hierarchical morphology exhibiting nano-, meso-, and micro-level features. A summary of the morphology of polymer/clay nanocomposites, and of corresponding microscopy and scattering techniques to determine such hierarchical morphology, was given by Vaia [33].

Characteristic parameters of various length scales are necessary in order to capture the special hierarchical morphology of nanocomposites. Recently, Nam and coworkers [13] have ascertained key features of the hierarchical morphology of intercalated polypropylene/clay nanocomposites (PPCN) using WAXS, SAX, TEM, polarized optical microscopy and light scattering. Fig. 8 shows a schematic of such a structure and illustrates the parameters of various hierarchies. The representative values of these parameters for a 4-wt% PPCN [13] are listed in Table 1. In an intercalated structure, where the inter-layer spacing ($d_{(001)}$ in Fig. 8) within a multi-layer stack of clay is usually 1–4 nm [33], the intra-layer polymer chains have a highly confined morphology. In the exfoliated or partially exfoliated systems, the particle separation (ξ_p) is about 20–50 nm [33], and is on the same order of crystal lamellae thickness. Such spacing, along with the detailed molecular interaction between clay and polymer, has an impact on the formation of crystallites in semi-crystalline polymer matrix (in particular, transcrystallization behavior of the matrix can be induced by the presence of the silicate layers), as observed in morphology studies on clay-filled polymer [34,35] as well as other filled polymers [36–39].

---

[2] The FEM-based RVE considered rectangular plate-like particles, whereas the Mori–Tanaka model considers more circular disk-like particles; therefore, the FEM model captures a larger particle overlap and strain shielding effect. Reality is likely somewhere in between, as the in-plane geometry of real particles is somewhat irregular.

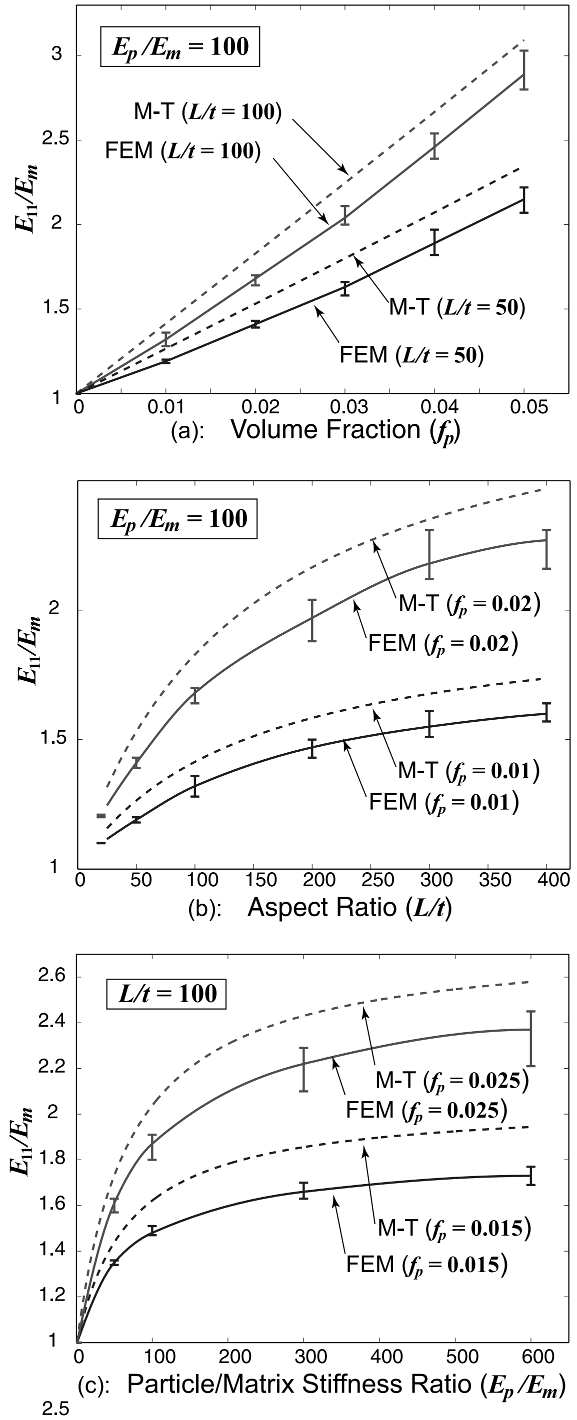

Fig. 4. Plane strain FEM results in comparison with the uniaxial results of Mori–Tanaka model: dependence of E_{11}/E_m on (a) f_p, for $L/t = 50$ and 100, $E_p/E_m = 100$; (b) L/t, for $f_p = 0.01$ and 0.02, $E_p/E_m = 100$; (c) E_p/E_m, for $f_p = 0.015$ and 0.025, $L/t = 100$. Each FEM data point is averaged over results of 10 random RVE realizations; the variation is reflected by error bars.

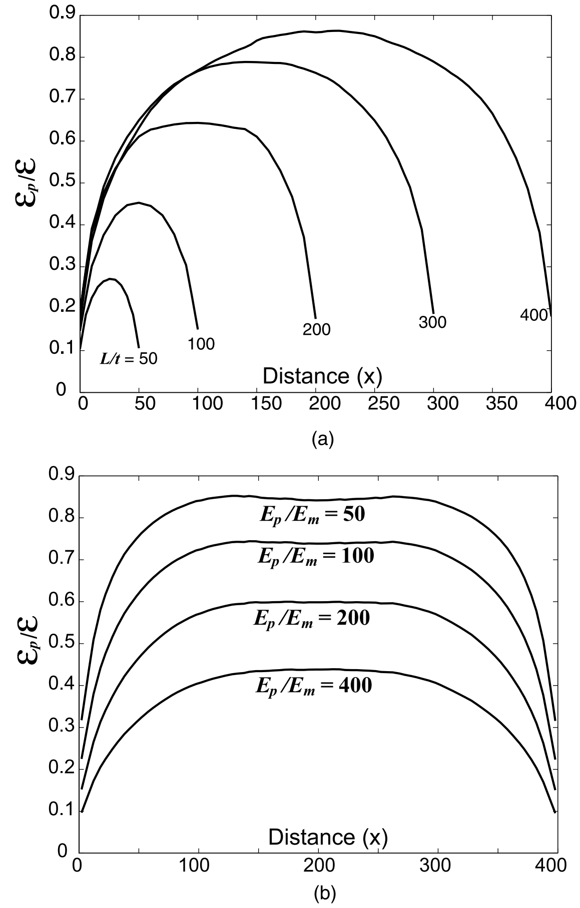

Fig. 5. Normalized particle strain distribution, averaged over all particles in the RVE. ε_p and ε denote the axial strain in the particle and the applied macroscopic strain ($\varepsilon = 0.5\%$), respectively, x is the distance along the particle, in units of particle thickness t. (a) Effect of particle aspect ratio, $L/t = 25, 50, 100, 200, 300$, and $400, f_p = 0.02, E_p/E_m = 100$; (b) Effect of particle/matrix stiffness ratio, $E_p/E_m = 50$, 100, 200, and 400, $f_p = 0.01$, $L/t = 400$.

Here, based on experimental observations together with modeling considerations, we identify two important sets of structural descriptors for the clay 'particle': primary descriptors and intermediate descriptors. The primary descriptors are the characteristic clay structural parameters directly related to processing, including the clay weight fraction (W_c), the clay atomic structure, the silicate interlayer spacing ($d_{(001)}$), the average number of silicate layers per clay stack (N), and the inter-layer gallery material. The intermediate descriptors are conventional composite material descriptors, including the particle volume fraction (f_p), the particle aspect ratio (L/t), and the ratio of particle (E_p) and matrix (E_m) stiffnesses, which may be anisotropic.

In order to develop predictive models of the macroscopic properties of polymer/nanoclay composites, a mapping of the primary descriptors to the intermediate descriptors of the nanoclay particle is needed, as presented next in Section 4. Micromechanical models are then constructed and utilized to compute the macroscopic mechanical properties of the polymer/clay nanocomposites in terms of the intermediate descriptors, as presented in Sections 5 and 6.

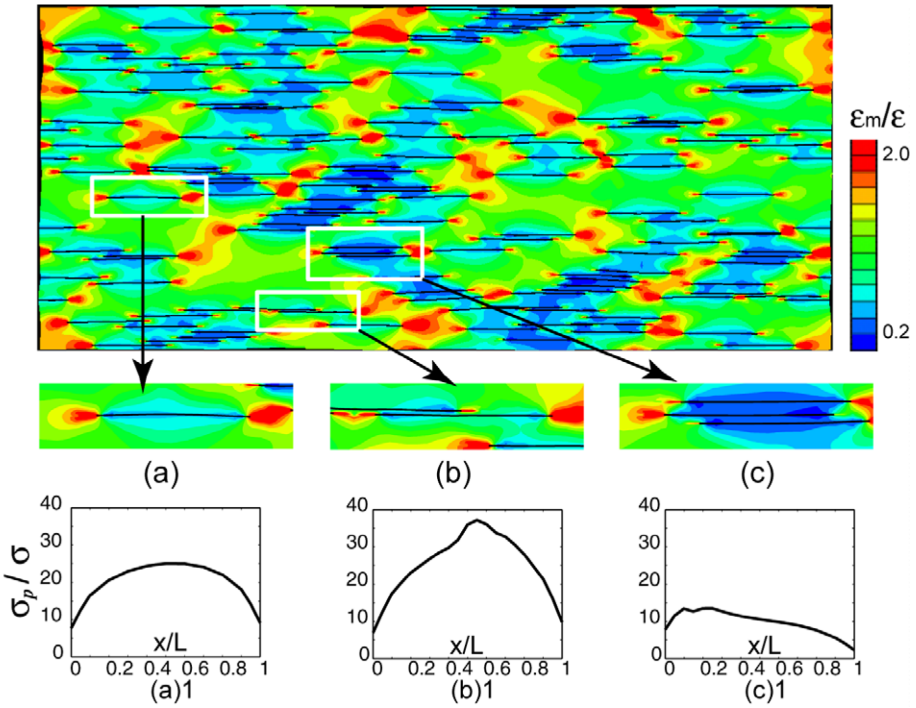

Fig. 6. Effect of strain shielding on load transfer efficiency (RVE with $f_p = 0.03$, $L/t = 100$, $E_p/E_m = 100$). (a) 'Isolated' particle; (b) partly 'overlapped' particle; (c) completely 'overlapped' particle. (a), (b), (c) 1: Normalized stress distributions in particle (a), (b), and (c), respectively; σ_p is the axial stress in the particle, σ is the macroscopic axial stress ($\sigma = 11.5$ MPa), x/L is the fractional distance along the particle, from left to right.

4. Effective representation of the nanoclay

Models for the macroscopic properties of composite materials operate on the 'particle' and the 'matrix'. The total spatial volume of the composite is well partitioned into the 'particle domain' and the 'matrix domain', as shown in Fig. 10(a); each domain is then treated as a homogeneous material, with certain elastic properties. However, a clearly defined 'particle domain' does not exist in intercalated polymer/clay nanocomposites; the layered structure of nanoclay (single silicate layers separated by inter-layer galleries) can be distinctly identified in TEM images, where example TEM micrographs of MXD6 nylon/clay nanocomposites with various weight percent clay are shown in Fig. 9.

Here, the idea of 'effective particle' is utilized in a way similar to that proposed in Brune and Bicerano [15]. The 'effective particle' is identified by a well-defined spatial volume, occupied by both the silicate layers *and* the inter-layer galleries, as shown in Fig. 10(b). We pay particular attention to the mechanical description of the silicate layers. The 'effective particle' is used as the basic element in continuum micromechanical models when assessing the influence of nanoclay content on overall nanocomposite properties.

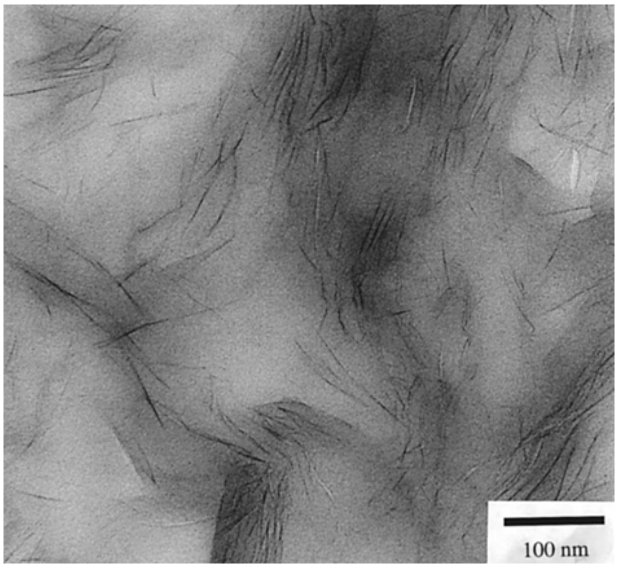

Fig. 7. TEM image of 10 wt% Cloisite 30A in a diamine-cured epoxy [32].

4.1. Structure of intercalated clay

Fig. 9 shows a highly magnified TEM image of MXD6 nylon/clay nanocomposite with 5.27-wt % clay. Analysis of the X-ray diffraction (XRD) pattern of this nanocomposite reveals a ~3-layer-crystalline structure with an average inter-layer spacing of $d_{(001)} = 4.1$ nm; in contrast, the corresponding organo-clay crystallite (without polymer penetration) has ~4 layers and an average inter-layer spacing of $d_{(001)} = 2.4$nm [40].

The hierarchical structure of the intercalated nanoclay is well shown in Fig. 11, where representations of the nanoclay at various lengthscales, such as 'particle', 'multi-layer stack', and 'repetitive lattice cell', in turn, are the fundamental elements of interest in analytical/numerical micromechanical

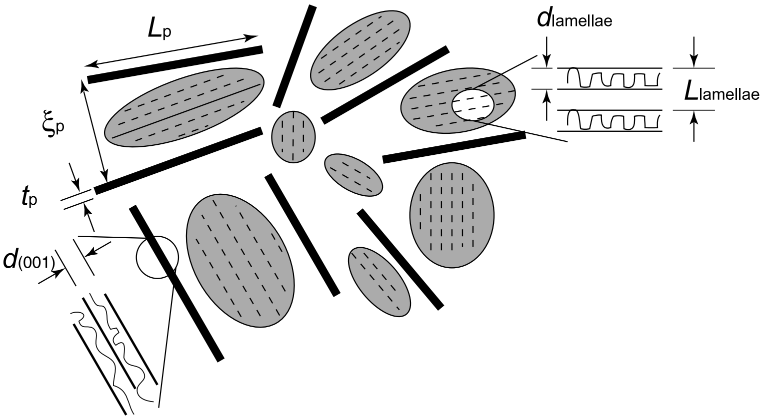

Fig. 8. Schematic of hierarchical morphology and characteristic parameters (adapted from Ref. [13]).

Table 1
Characteristic values for hierarchical structure-describing parameters for 4-wt% PPCN, [13] (see also Fig. 8)

Symbol	Characteristic parameter	Typical value (nm)
L_p	Length of the dispersed clay particles	130–180
ξ_p	Correlation between particles (inter-particle spacing)	40–60
t_p	Thickness of the clay particles	7–9
$d_{(001)}$	Inter-layer spacing of the (001) plane in intercalated clay	3
$d_{lamellae}$	Average lamellae thickness of polymer matrix crystallite	7
$L_{lamellae}$	Long-period lamellae thickness of polymer crystallite	15

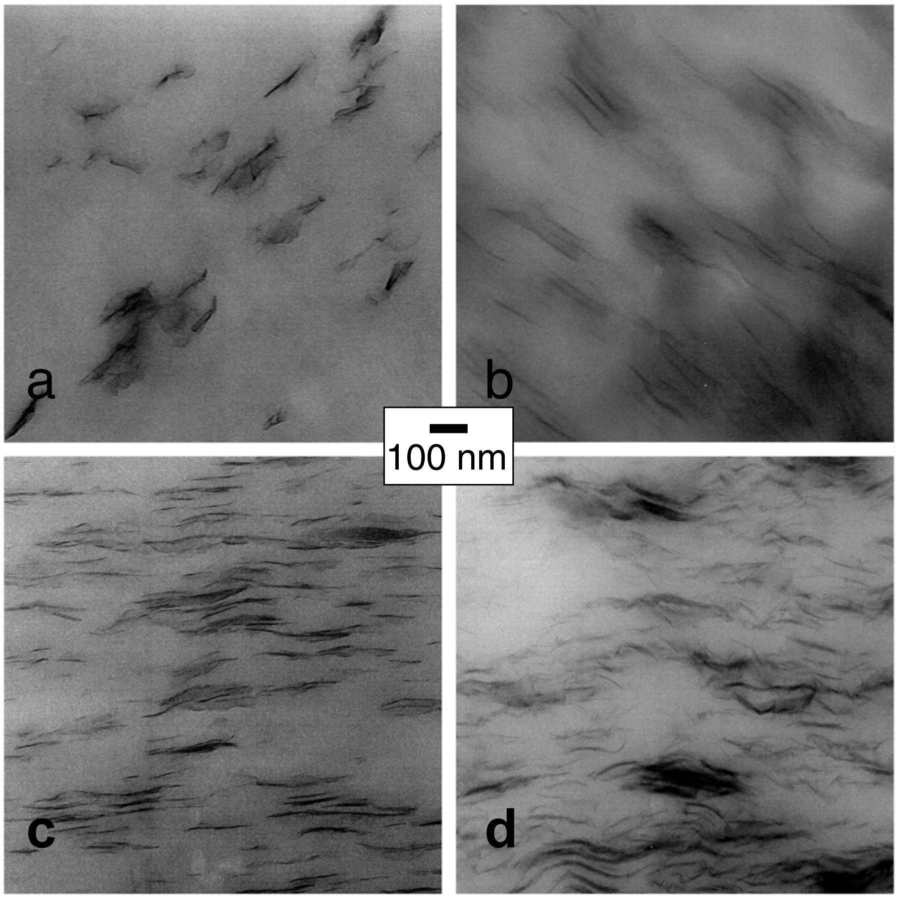

Fig. 9. TEMs of MXD6 nylon/clay nanocomposite with various clay contents: (a) 1.1 wt%, (b) 3.67 wt%, (c) 4.17 wt%, (d) 5.27 wt%.

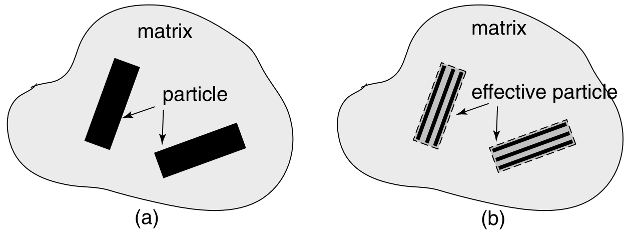

Fig. 10. Illustrations of the ‘particle’ and ‘matrix’ domains in (a) conventional composite, (b) nanocomposite. The dash-lined boxes in (b) indicate spatial domain of the ‘effective particle’.

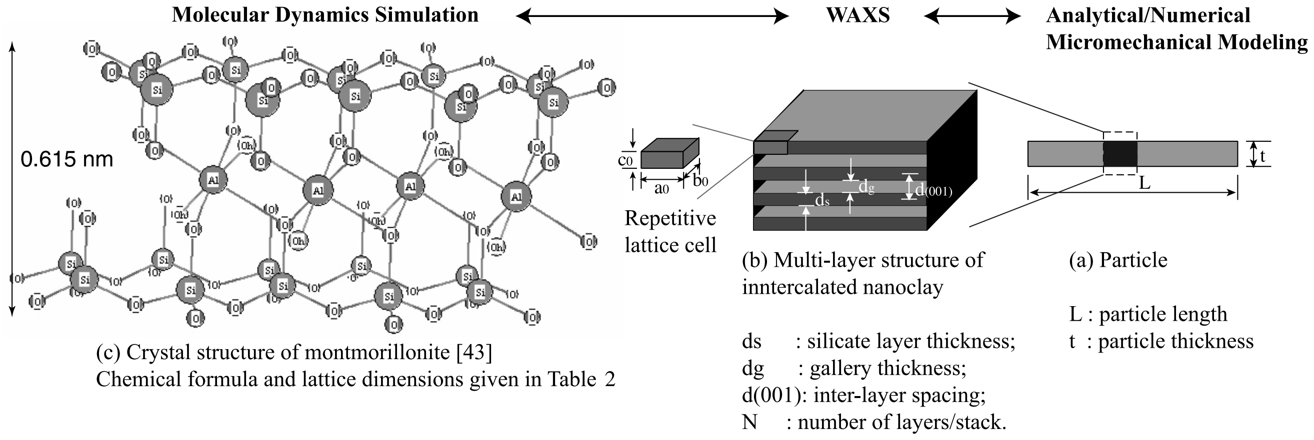

(c) Crystal structure of montmorillonite [43]
Chemical formula and lattice dimensions given in Table 2

(b) Multi-layer structure of inntercalated nanoclay

ds : silicate layer thickness;
dg : gallery thickness;
d(001): inter-layer spacing;
N : number of layers/stack.

(a) Particle

L : particle length
t : particle thickness

Fig. 11. Hierarchical structure of the nanoclay.

modeling, WAXS, and molecular dynamics simulation. While the ‘particle’ in micromechanical modeling is simply characterized by its aspect ratio (geometry) and elastic properties, the underlying structure of the nanoclay must be characterized and approximated in order to obtain reasonable estimates of the effective geometry and properties of the ‘particle’; indeed, both WAXS and molecular dynamics simulation results are indispensable assistances to micromechanical modeling of polymer/clay nanocomposites.

For simplicity, the internal structure of an intercalated clay particle is idealized as a multi-layer stack containing N single silicate sheets (each sheet has an area A, an effective thickness d_s and mass M) with uniform inter-layer spacing $d_{(001)}$, as shown in Fig. 11(b). Separating adjacent sheets is a so-called gallery layer comprising both surfactants and polymer matrix chains that have penetrated the inter-silicate layers during various stages of synthesis and processing. The particle thickness t can be related to the internal structural parameters N and $d_{(001)}$ through

$$t = (N-1)d_{(001)} + d_s, \tag{4}$$

where d_s is the silicate sheet thickness. A similar approach is used in Ref. [15] where effective particle thickness is expressed in terms of multiples of sheet thickness and gallery thickness. Note that there is some ambiguity in assigning a precise value to thickness for nanoparticles of atomic level thickness such as carbon nanotubes (CNT) and nanoclay sheets, especially with regard to providing accurate representation of mechanical properties using continuum level models (e.g. [41–43]). Therefore, we choose to represent the effective particle thickness in terms of the measurable interlayer spacing $d_{(001)}$ and a single sheet thickness d_s, where d_s will be defined later to be a *mechanical thickness* of the sheet[3].

Each individual silicate sheet further consists of n repetitive lattice cells, each of area A_0, thickness d_s, and molecular weight M_0. The crystal structure of a montmorillonite lattice cell used in molecular dynamics simulations [43] is shown in Fig. 11(c). Table 2 summarizes its characteristic parameters. This model framework will later be used to determine effective properties of the clay ‘particle’, including determination of the particle aspect ratio, volume fraction of the particle (in terms of clay weight fraction), and particle stiffness (which may be anisotropic). Note that the subscripts *silicate* and *gallery* are used to denote the properties of the silicate sheet, and the gallery, respectively. The subscripts p and m are used to denote the properties of the effective particle and the matrix, respectively.

Important parameters of the clay structure are the number of silicate sheets per unit particle thickness:

$$\chi_N = \frac{N}{t} = \frac{N}{(N-1)d_{(001)} + d_s}; \tag{5}$$

which can be alternatively expressed as the volume fraction

---

[3] Furthermore, surrounding the exterior silicate layers is a special morphology material composed of some blend of surfactants and confined matrix polymer chains, which rapidly transitions to 100% matrix material with increasing distance from the particle. For present purposes, we neglect these special regions and features, and simply include them within the matrix volume and matrix properties. The proposed approach can be straight forwardly extended to account for these features within the definition of the ‘effective particle’.

Table 2
Molecular characterization of montmorillonite lattice cell (Manevitch and Rutledge, [43])

	Unit	Symbol	Value
Chemical structure			$2\{\mathrm{Al_2Si_4O_{10}(OH)_2}\}$
Planar dimensions	nm	(a_0, b_0)	(0.53, 0.92)
Planar area	$(\mathrm{nm})^2$	$A_0 = a_0 b_0$	0.49
Thickness	nm	$c_0 (c_0 = d_\mathrm{s})$	0.615
Molecular weight	g/mol	M_0	720

of silicate in the effective particle

$$\chi = \frac{V_\mathrm{silicate}}{V_\mathrm{p}} = \frac{N d_\mathrm{s}}{(N-1)d_{(001)} + d_\mathrm{s}}$$

$$= \frac{1}{\left\{\left(1 - \frac{1}{N}\right)\left(\frac{d_{(001)}}{d_\mathrm{s}}\right) + \frac{1}{N}\right\}}, \tag{6}$$

where V_silicate and V_p are the volumes assigned to the silicate sheets in a stack and to the effective particle, respectively. The dimensionless quantity χ is a function of two internal parameters of the nanoclay particle: its number of silicate sheets, N, and the relative inter-layer swelling, $d_{(001)}/d_\mathrm{s}$. Fig. 12 shows decreases in silicate volume fraction χ with increasing $d_{(001)}/d_\mathrm{s}$ for different N-values; the observation that the case $N = 1$ stands out from the others ($N > 1$) suggests significant distinction in structure-related effective particle properties between exfoliated systems and intercalated systems (similar effects on χ_N are to be expected since $\chi_N = \chi/d_\mathrm{s}$).

4.2. Properties of the effective clay particle

The effective particle is 'equivalent' to the multi-layer stack shown in Fig. 11(b) in the sense that it possesses the same L/t, f_p, and overall mechanical properties as the discrete stack. With Eq. (4), L/t can be calculated as

$$\frac{L}{t} = \frac{L}{(N-1)d_{(001)} + d_\mathrm{s}}. \tag{7}$$

Eq. (7) can be further written in terms of χ_N and N as

$$\frac{L}{t} = \left(\frac{L}{N}\right)\chi_N. \tag{8}$$

4.2.1. Conversion from clay weight fraction (W_c) to particle volume fraction (f_p)

Experimental studies (e g. [3], [44]) detail and plot property enhancement data in terms of weight fraction clay. Since the clay content is provided in terms of weight fraction W_c (ash weight), it is necessary to establish a quantitative connection between W_c and the volume fraction of the 'effective particle' f_p, an important parameter in micromechanical models.

First, consider a two-phase composite consisting of matrix and particles (or 'effective particles' in the case of a nanocomposite); the particle volume fraction f_p and particle weight fraction W_p are related according to

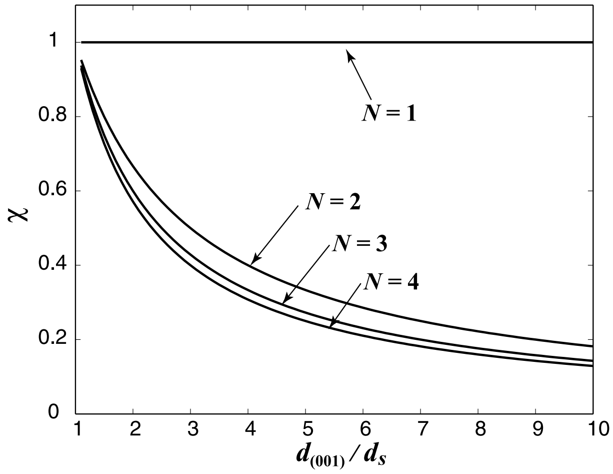

Fig. 12. Dependence of particle silicate volume fraction χ on clay structural arameters N and $d_{(001)}/d_\mathrm{s}$.

$$f_\mathrm{p} = \frac{W_\mathrm{p}/\rho_\mathrm{p}}{W_\mathrm{p}/\rho_\mathrm{p} + (1 - W_\mathrm{p})/\rho_\mathrm{m}}, \tag{9}$$

where ρ_p and ρ_m are the mass densities of the particle and the matrix, respectively.

For an intercalated nanocomposite, W_c differs from the 'particle' weight fraction W_p, since the 'particle' consists of both silicate sheets and the inter-layer galleries. The two quantities are related through

$$\frac{W_\mathrm{p}}{W_\mathrm{c}} = \frac{\rho_\mathrm{p} V_\mathrm{p}}{\rho_\mathrm{silicate} V_\mathrm{silicate}} = \left(\frac{\rho_\mathrm{p}}{\rho_\mathrm{silicate}}\right) \Big/ \left(\frac{V_\mathrm{silicate}}{V_\mathrm{p}}\right)$$

$$= \frac{\rho_\mathrm{p}}{\rho_\mathrm{silicate}} \frac{1}{\chi} \equiv \alpha, \tag{10}$$

where ρ_silicate is the mass density of the silicate sheet, and the ratio $W_\mathrm{p}/W_\mathrm{c}$ is defined as α.

Taking $W_\mathrm{p} = \alpha W_\mathrm{c}$ into Eq. (9), we can write f_p as a function of W_c

$$f_p = \frac{W_\mathrm{c}/\rho_\mathrm{p}}{W_\mathrm{c}/\rho_\mathrm{p} + (1/\alpha - W_\mathrm{c})/\rho_\mathrm{m}}. \tag{11}$$

When W_c is small, as it often is for the nanocomposite, Eq. (11) can be linearized as

$$f_p \approx \left(\frac{\alpha \rho_\mathrm{m}}{\rho_\mathrm{p}}\right) W_\mathrm{c} = \left(\frac{\rho_\mathrm{m}}{\rho_\mathrm{p}} \cdot \frac{\rho_\mathrm{p}}{\rho_\mathrm{silicate}} \cdot \frac{1}{\chi}\right) W_\mathrm{c}$$

$$= \left(\frac{\rho_\mathrm{m}}{\rho_\mathrm{silicate}} \cdot \frac{1}{\chi}\right) W_\mathrm{c}. \tag{12}$$

The density ρ_silicate can be calculated from the montmorillonite lattice parameters given in Table 2,

$$\rho_\mathrm{silicate} = \rho_\mathrm{lattice} = \frac{M_0}{A_0 d_\mathrm{s}} = \left(\frac{2.44}{d_\mathrm{s}}\right) \mathrm{nm}\ g/(\mathrm{cm})^3. \tag{13}$$

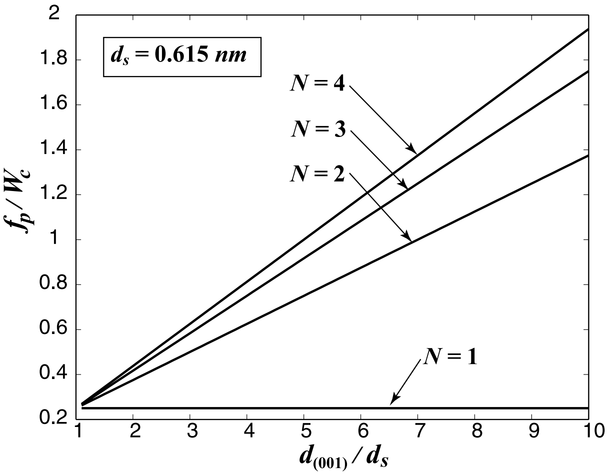

Fig. 13. Dependence of f_p/W_c on clay structural parameters N and $d_{(001)}/d_s$.

Taking Eq. (13) and an assumed value of $\rho_m = 1.0\ g/(cm)^3$ into Eq. (12), we have

$$f_p = \left(\frac{0.41 d_s}{nm}\right)\frac{W_c}{\chi} = \left(\frac{0.41}{\chi_N} W_c\right)\ \mathrm{nm}^{-1}. \tag{14}$$

The conversion ratio f_p/W_c given in Eq. (14) is plotted as a function of N and $d_{(001)}/d_s$ in Fig. 13 (note that this ratio is in proportion to the inverse of χ, which is plotted in Fig. 12). Beall [45] took $N = 1$ and $d_s = 1$ nm, and obtained $f_p = 0.4W_c$, consistent with the present result; however, other particle structures can lead to f_p/W_c ratios > 1, reflecting the increased spatial extent of swollen intercalated stacks.

4.2.2. *Effective anisotropic mechanical properties of the particle*

Considering the multi-layer clay particle as a laminate (with isotropic silicate sheets and orthotropic polymeric galleries), as shown in Fig. 14, the overall elastic properties of the effective particle can be estimated as

$$E_{p,11} = \chi_N E_{\mathrm{silicate}} d_s + (1-\chi)E_{\mathrm{gallery},11}$$

$$= \chi E_{\mathrm{silicate}} + (1-\chi)E_{\mathrm{gallery},11}, \tag{15}$$

$$E_{p,22} = \frac{E_{\mathrm{silicate}}E_{\mathrm{gallery},22}}{(1-2\beta\nu_{\mathrm{gallery}})[(1-\chi)E_{\mathrm{sillicate}} + \chi E_{\mathrm{gallery},22}]},\ \text{with}$$

$$\beta = \frac{E_{\mathrm{silicate}}\nu_{\mathrm{gallery}} - E_{\mathrm{gallery}}\nu_{\mathrm{silicate}}}{(1-\nu_{\mathrm{gallery}})E_{\mathrm{silicate}} + (1-\nu_{\mathrm{silicate}})E_{\mathrm{gallery}}} \tag{16}$$

$$\nu_{p,12} = \chi\nu_{\mathrm{sillicate}} + (1-\chi)\nu_{\mathrm{gallery},12}, \tag{17}$$

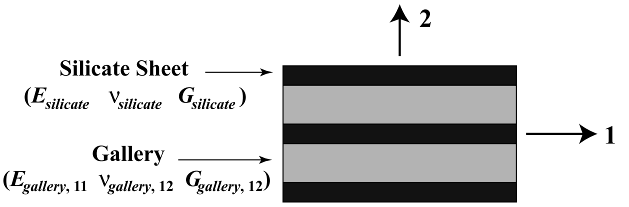

Fig. 14. Schematic of a lamina with two phases: silicate sheet and gallery.

$$G_{p,12} = \frac{G_{\mathrm{silicate}}G_{\mathrm{gallery},12}}{(1-\chi)G_{\mathrm{silicate}} + \chi G_{\mathrm{gallery},12}} \tag{18}$$

Manevitch and Rutledge [43] calculated the elastic behavior of a single silicate sheet from molecular dynamics (MD) simulations. The MD simulations compute the membrane stiffness, $E_{\mathrm{silicate}}d_s = 246 \sim 258$ N/m. In order to determine a value for the modulus E_{silicate}, one must divide the membrane stiffness by the sheet thickness. There is ambiguity is assigning a thickness to a particle of one lattice unit thickness, since it is unclear how to assess the proper radius of influence of an atom in this regard. This issue has been successfully addressed in the CNT literature [41] where a combination of atomistic simulations of membrane and bending deformation act to identify a *mechanical thickness* (the thickness value that will provide accurate representation of the mechanical behavior of the atomic-thickness lamina, both stretching and bending, when using continuum-level models). Pantano et al. [42] have demonstrated that using the CNT wall (modulus, thickness) pair computed in this manner, together with shell theory, enables the prediction of a wide range in mechanical behavior of single and multi-wall CNTs. Manevitch and Rutledge [43] follow an analogous approach to extract a (modulus, thickness) pair for the montmorillonite silicate sheet from their MD simulations, which sampled both membrane and bending behavior of the sheet. Their calculations give a membrane stiffness which can be further broken down to a (thickness, modulus) pair of $d_s = 0.615$ nm and $E_{\mathrm{silicate}} = 400\text{–}420$ GPa, based on the silicate layer bending stiffness deduced from buckling behavior.

The elastic properties of the gallery are undetermined; however, it is speculated that $E_{\mathrm{gallery}}/E_{\mathrm{silicate}} \ll 1$, and $G_{\mathrm{gallery}}/G_{\mathrm{silicate}} \ll 1$, which will severely reduce the overall $E_{p,22}$ and $G_{p,12}$ of the effective particle.

In some instances, the effect of particle anisotropy can be neglected (see Section 5 for discussion). In those cases, only two independent particle elastic constants, E_p and ν_p, are required. We approximate E_p with $E_{p,11}$, and ν_p with $\nu_{p,12}$. Taking $E_{\mathrm{silicate}}d_s = 250$ N/m [43], $E_m = 4$ GPa,[4] and assuming $E_{\mathrm{gallery}} \ll E_{\mathrm{silicate}}$, the particle/matrix stiffness ratio can be estimated as

$$\frac{E_p}{E_m} = \frac{\chi_N(E_{\mathrm{silicate}}d_s)}{E_m} = (62.5\chi_N)m. \tag{19}$$

The particle/matrix stiffness ratio given in Eq. (19) is proportional to the number of silicate sheets per unit particle thickness; we plot the stiffness ratio here in Fig. 15, as a function of N and $d_{(001)}/d_s$, to emphasize the dramatic decrease in 'particle' stiffness accompanying the morphological transition from *complete exfoliation* ($N = 1$) to

---

[4] Here, we take the matrix to be MXD6 nylon with modulus of Em = 4 GPa. Obviously, any matrix can be studied by looking at different matrix moduli.

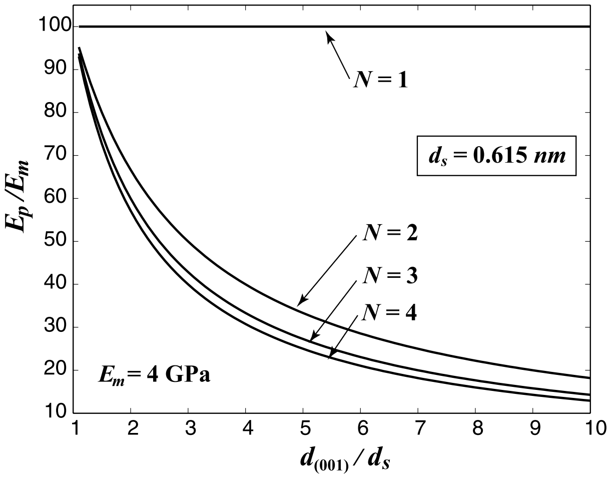

Fig. 15. Dependence of longitudinal particle modulus E_p/E_m on clay structural parameters N and $d_{(001)}/d_s$ ($E_m = 4$ GPa).

intercalation ($N \geq 2$). However, it will be shown that the overall modulus ratio, E_{11}/E_m, will not show a correspondingly dramatic decrease when the morphology transitions from complete exfoliation to intercalation, mainly because of compensating effects of both f_p/W_c and L/t, which can be appreciated by consideration of Fig. 13.

5. Micromechanical modeling of intercalated polymer/nanoclay composite

The hierarchical morphology of intercalated nanoclay and surrounding polymer add constitutive as well as structural complexity to nanocomposite modeling. Here, we focus on structure-constitutive modeling of the nanoclay. While the analytical micromechanical models reviewed in Section 2.1 require effective representation of the layered-nanoclay as a homogeneous isotropic ‘particle’, FEM-based micromechanical simulations allow the intercalated clay particle to be modeled in various levels of detail—an effective ‘particle’ with anisotropic elastic properties, or even as a laminate consisting of silicate and gallery. The tasks of this section are to explore these different structural and constitutive models of the nanoclay; to contrast the load transfer performances and overall composite moduli predicted by each model; and to validate the use of an ‘effective particle’ representation in analytical micromechanical modeling of polymer/clay nanocomposites. An exemplar three-layer clay structure is chosen for illustration purposes.

5.1. Constitutive models

Due to the hierarchical morphology of intercalated nanoclay (Section 3), we consider three possible structural/constitutive models of the volume to be assigned to the clay ‘particle’: ‘*discrete stack*’, ‘*anisotropic particle*’ and ‘*isotropic particle*’, as shown in Fig. 16. The ‘*discrete stack*’ (a) is a laminate composite consisting of N silicate layers of thickness d_s and inter-layer spacing $d_{(001)}$, and $(N-1)$ gallery layers of thickness $d_g = d_{(001)} - d_s$. Each of the silicate and gallery layers are assigned distinct elastic properties. The ‘*anisotropic particle*’ (b) is a homogenized representation of (a), whose overall dimensions and anisotropic elastic properties ($E_{p,11}, E_{p,22}, G_{p,12}, G_{p,13}, \nu_{p,12}$) can be calculated from Eq. (8) and Eqs. (15)–(19); the ‘isotropic particle’ (c) is a further simplification of (b), characterized simply by isotropic elastic constants E_p and ν_p.

Table 3
Elastic constants of the two components in the ‘discrete stack’, shown in Fig. 12(a) ($N = 3$, $d_{(001)}/d_s = 4$, $L/t = 200/9 \Rightarrow \chi = 1/3$); the silicate layers are modeled as isotropic material whereas galleries are orthotropic ($E_{\text{gallery},11} = E_{\text{gallery},22} = E_{\text{gallery},33}$, $\nu_{\text{gallery},12} = \nu_{\text{gallery},13} = \nu_{\text{gallery},23}$, $G_{\text{gallery},12} = G_{\text{gallery},13} = G_{\text{gallery},23}$)

	E_{silicate} (GPa)	ν_{silicate}	$E_{\text{gallery},11}$ (GPa)	$\nu_{\text{gallery},12}$	$G_{\text{gallery},12}$ (GPa)
(a) Discrete stack	400	0.20	4.0	0.35	0.015

For comparison purposes, we consider a specific model intercalated clay structure with $N = 3$, $d_{(001)}/d_s = 4$, and $L/t = 200/9$, resulting via Eq. (6) in a ‘particle’ silicate volume fraction $\chi = 1/3$ (definition of χ given in Eq. (6)). Elastic constants of the silicate [43] and those assumed for the gallery are given in Table 3. Corresponding effective mechanical properties of the homogenized ‘anisotropic particle’ and ‘isotropic particle’, calculated from Eqs. (15)–(19), are listed in Table 4. Matrix material parameters are assumed to be $E_m = 4.0$ GPa, $\nu_m = 0.35$ (shear modulus $G_m = E_m/2(1+\nu_m) = 1.48$ GPa).

We assume that the orthotropic gallery has a very low shear modulus ($G_{\text{gallery},12} = G_m/100$) in order to study the effect of anisotropy. As a result, $G_{p,12}$ of the homogenized ‘anisotropic particle’ is much smaller than that of the homogenized ‘isotropic particle’. Recalling the shear-lag analysis discussed in Section 2.2.2, profound differences in the efficiency of load transfer into the interior of these modeled ‘particles’ are expected.

5.2. Results

A 2D plane strain RVE containing $f_p = 0.05$ volume fraction of particles with $L/t = 200/9$ is constructed; the geometry of the particle is designed such that it can

Table 4
Elastic constants of the homogenized effective ‘anisotropic particle’ and ‘isotropic particle’, shown in Fig. 16(b) and (c), respectively (calculated from Eqs. (15)–(19))

	$E_{p,11}$ (GPa)	$E_{p,22}$ (GPa)	$\nu_{p,12}$	$G_{p,12}$ (GPa)	$G_{p,13}$ (GPa)
(b) Anisotropic particle	136	19.5	0.28	0.067	57
(c) Isotropic particle	136	136	0.28	53	53

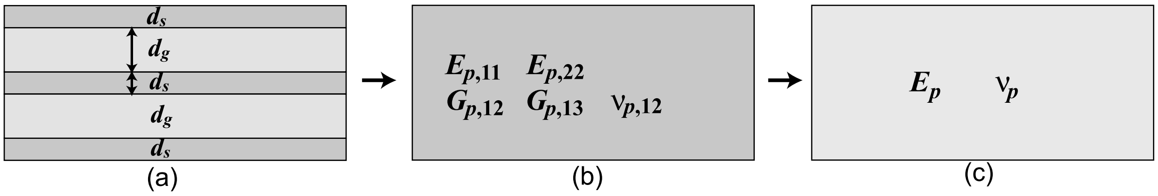

Fig. 16. Constitutive and structural models of the clay particle: (a) discrete stack; (b) anisotropic homogenized particle; (c) isotropic homogenized particle. For idealization (a), the material properties are indicated in Fig. 14.

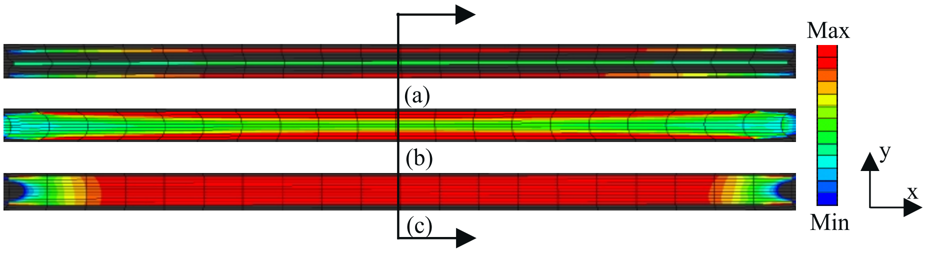

Fig. 17. Axial stress distributions in a particular particle under 0.5% axial loading ($f_\mathrm{p} = 0.05$, $L/t = 200/9$). In separate simulations, the clay particle is modeled, in turn, as: (a) discrete stack; (b) homogenized anisotropic particle; (c) homogenized isotropic particle. (Max/Min axial stress within the silicate domain for (a): 800 MPa/400 MPa; max/min axial stress within the particle domain for (b) and (c): 200 MPa/100 MPa).

accommodate precisely the intercalated clay structures characterized in Table 3 The three geometric/constitutive models of the particles, described in Fig. 16 and Tables 3 and 4, are applied to the same RVE. Perfect bonding is assumed for all material interfaces, including matrix/particle, matrix/silicate, silicate/gallery and gallery/matrix.

Load transfer from the matrix to the particle is strongly affected by the different shear properties of the three particle models. Fig. 17 shows the tensile stress contours in one specific particle in the RVE, when each of the three structural/constitutive models of the particle is applied in turn; the RVE is subjected to 0.5% macroscopic axial strain. Both the differences and the similarities between Fig. 17(a), (b) and (c) can be interpreted through shear-lag analysis. In case (a), only a small amount of load is transferred to the middle silicate layer, due to the low shear modulus of the galleries; similarly, in case (b) the low $G_{\mathrm{p},12}$ of the homogenized ‘anisotropic particle’ results in very low stress inside the particle; however, in case (c) the load is efficiently transferred to the interior of the particle because of the substantially higher G_p of the homogenized ‘isotropic particle’.

Despite such model-based differences in local stress fields within the ‘particle’ domain, the macroscopic responses of the RVE are rather close: the overall stiffness enhancement E_{11}/E_m, predicted with use of models (a), (b) and (c), are perhaps surprisingly close, 1.41, 1.37, and 1.44, respectively. But such results are not surprising if we compare the net axial force carried by each particle instead of the axial stresses. Fig. 18 depicts the axial stress distribution through the thickness of each particle model, at the central cross section indicated in Fig. 17. The tensile force carried by the particle can be obtained by integrating the axial stress over the cross-section (along the y-axis, in this case). The large stress in the outer discrete silicate layers is counteracted by very low stress in the galleries, so the tensile force carried by a silicate/gallery laminate differs little from that carried by its effective representations.

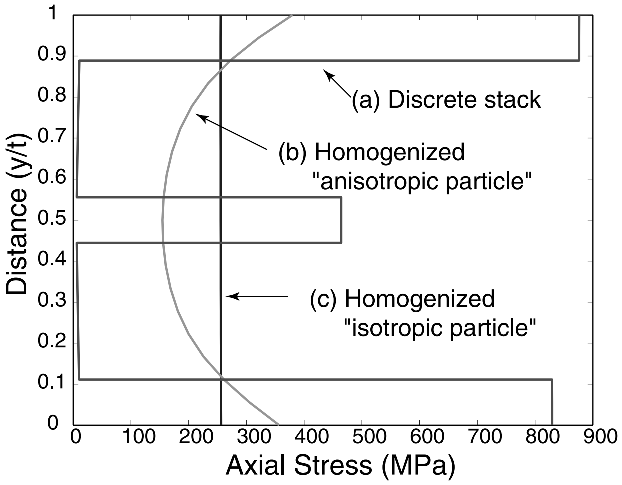

Fig. 18. Axial stress distributions along the mid-particle cross-section, marked in Fig. 17. The integrated tensile forces carried by each particle model are similar, even though the stress distributions differ substantially.

We chose a relatively heavily loaded nanocomposite ($f_\mathrm{p} = 0.05$) and assumed a very low gallery shear modulus ($G_{\mathrm{gallery},12} = G_\mathrm{m}/100$); the differences in both the local stress distribution and the macroscopic composite response caused by different geometric/constitutive modeling of the clay particle diminish with decreasing f_p or increasing $G_{\mathrm{gallery},12}/G_\mathrm{m}$.

Although the idealized ‘isotropic particle’ (as is utilized in many micromechanical models, including Halpin–Tsai and Mori–Tanaka) seems to be a sufficiently good representation of the intercalated nanoclay when axial deformation of perfectly aligned particle composite is concerned, it is important to note that this approximation is inherently conditional. Failure of the ‘isotropic’ model to capture the low $G_{\mathrm{gallery},12}$ will cause significant consequences under circumstances of off-axial straining or particle misalignment. For illustration purposes, the same RVE utilized in the axial tensile deformation simulations discussed above is subjected to simple shear deformation with the three particle geometry/constitutive models. The calculated overall shear modulus corresponding to the 'discrete stack', 'anisotropic particle', and 'isotropic particle' are $G_{12}/G_m = 0.71$, 0.73, and 1.57, respectively. The 'isotropic' model predicts a false increase in overall G_{12}, as a result of the high G_p of the 'isotropic particle'. These simple shear results suggest that an anisotropic (instead of isotropic) 'particle' should be used to effectively represent the intercalated nanoclay when particle misalignment or curvature is under concern.

In summary, we claim that for the purpose of determining the particle aspect ratio and stiffness, it is reasonable to model the intercalated clay as a homogeneous isotropic particle (at least in cases where the particles are well aligned, the applied loading is axial, and the macroscopic tensile modulus is of interest). The justification of using a homogenized isotropic particle in micromechanical modeling of nanocomposites, in turn, suggests the potential contribution of conventional composite models presented in Section 2.

6. Application of multi-scale modeling

Through previous sections, multi-scale micromechanical modeling of the polymer/clay nanocomposite has been developed for internal consistency. In summary, clay structural parameters (L, N, $d_{(001)}$) extracted from XRD and/or TEM are mapped into effective 'particle' properties (L/t, f_p/W_c, E_p/E_m), which are then used as model parameters in analytical or numerical micromechanical composite models to calculate macroscopic stiffness of the nanocomposite. Here, this modeling scheme is applied to various polymer–clay nanocomposite systems; FEM predictions of the composite modulus based on the 'effective particle' are compared with a series of experimental data; finally the effects of processing on the overall mechanical properties are estimated.

6.1. Parametric study of the effect of (N, $d_{(001)}$) on composite modulus

Fig. 19 depicts the influence of internal clay structural parameters ($N, d_{(001)}$) on the macroscopic modulus of the nanocomposite; Eqs. (8), (14) and (19) are used to calculate the micromechanical model parameters, where a silicate sheet thickness d_s of 0.615 nm[5] is used in determining χ_N, the particle length L is assumed to be 200 nm in (a)–(c), and 100 nm in (d). The Mori–Tanaka model (Eq. (2)) is used to predict the overall composite modulus. The effects of (N, $d_{(001)}$) on (L/t, f_p/W_c, E_p/E_m) corresponding to Fig. 19 are summarized in Table 5.

Table 5
Effect of primary descriptors (N, $d_{(001)}$) on intermediate model descriptors ($L/t, f_p/W_c$, E_p/E_m), calculated according to Eqs. (8), (14) and (19) (see also Fig. 19)

N	$d_{(001)}/d_s$	L/t	f_p/W_c	E_p/E_m
Effect of N on model parameters				
4	6.5	16	1.28	19.5
3	6.5	23	1.17	21.4
2	6.5	43	0.94	26.7
1		325	0.25	100
Effect of $d_{(001)}/d_s$ on model parameters				
2	1.6	124	0.328	76.2
2	8.1	36	1.14	21.9
5	1.6	43	0.375	66.6
5	4.9	16	1.03	24.4
5	8.1	10	1.68	14.9

E_{11}/E_m is plotted as a function of W_c and N at a fixed $d_{(001)}$ in Fig. 19(a). The strong dependence of E_{11}/E_m on N is clearly demonstrated; at a fixed W_c, E_{11}/E_m increases with decreasing N; the amount of increase gradually expands as $N \rightarrow 1$; however, no dramatic change occurs in this limit. At a given W_c, as N decreases, L/t and E_p increase, which both act to increase E_{11}, whereas f_p decreases, which acts to decrease E_{11}. The increases in L/t and E_p have a stronger effect than the decrease in f_p. Fig. 19(b) depicts the effect of $d_{(001)}/d_s$ on the macroscopic modulus for two different values of N: $N = 2$, and $N = 5$. Compared with N, the influence of $d_{(001)}/d_s$ on E_{11}/E_m is rather small, and depends on the specific value of N. In general, for a fixed N and W_c, E_{11}/E_m increases with increasing $d_{(001)}$ (note that a maximum $d_{(001)}$ of 5 nm is studied; values larger than this are not considered to be of interest); this increase is rather negligible when N is small; however, when the nanocomposite is highly intercalated (e.g. $N = 5$), the increase of a few nanometers in $d_{(001)}$ can cause a considerable increase in E_{11}/E_m. At a given W_c, as $d_{(001)}$ increases, both L/t and E_p decrease, acting to decrease E_{11}, whereas f_p increases, acting to increase E_{11}. The increase due to f_p prevails over the decreases from L/t and E_p.

Note that in order to determine E_p/E_m, Eq. (19) used a matrix modulus of $E_m = 4$ GPa, which leads to an $E_{\mathrm{silicate}}/E_m = 100$ (taking $d_s = 0.615$ nm, $E_{\mathrm{silicate}} = 400$ GPa). However, the modulus of different polymers vary from order MPa (elastomers; amorphous polymers above their glass transition temperature) to order GPa (semicrystalline polymers, glassy polymers, and epoxies) and thus $E_{\mathrm{silicate}}/E_m$ for different polymer–clay nanocomposite systems has a wide range, from $\sim 10^5$ down to $\sim 10^2$. To emphasize the strong effect of E_p/E_m on composite modulus, shown earlier in Figs. 1(c) and 4(c), we plot in Fig. 19(c) the effect of N for two values of $E_{\mathrm{silicate}}/E_m$. For a

---

[5] Here, we choose this particular value of $d_s = 0.615$ nm since it pairs with the silicate modulus of $E_p = 400$ GPa, calculated from molecular dynamics simulation [43]. In view of the substantial equivalence of the various particle structure/property idealizations shown in Section 5, equivalent results could be and were obtained with larger d_s values, along with consistently reduced silicate moduli.

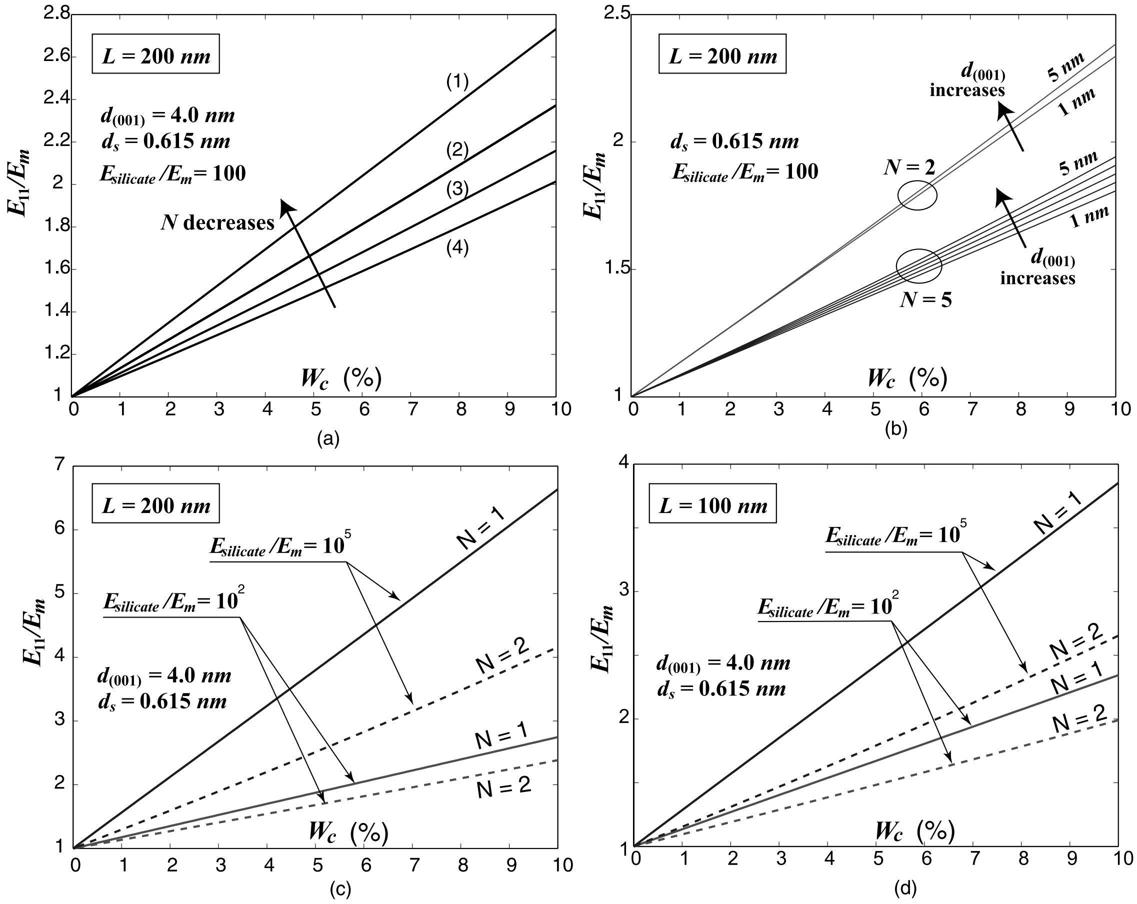

Fig. 19. Effect of clay structural parameters (N, $d_{(001)}$) on the macroscopic modulus, predicted by the Mori–Tanaka model; model parameters calculated from Eqs. (8), (14) and (19), $d_s = 0.615$ nm, $L = 200$ nm for (a), (b) and (c), $L = 100$ nm for (d). (a) Effect of N at fixed $d_{(001)}$: $d_{(001)} = 4.0$ nm. (b) Effect of $d_{(001)}$ at two fixed values $N = 2$ and $N = 5$. (c) Effect of matrix stiffness for exfoliated ($N = 1$) and intercalated ($N = 2$) systems, with $L = 200$ nm. (d) Effect of matrix stiffness for exfoliated and intercalated systems, with $L = 100$ nm.

given exfoliated and well aligned clay content W_c, the stiffness enhancement is much more dramatic for a compliant matrix where E_p/E_m is of order 10^5 (i.e. elastomers or thermoplastics at temperatures above T_g) than a stiff matrix where $E_p/E_m = 10^2$. In particular, if we examine the case of 4 wt% clay, under fully exfoliated and fully aligned conditions, the elastomer nanocomposite modulus is over 3 times that of its matrix, whereas the glassy polymer nanocomposite modulus is only ~50% higher than its matrix. This prediction is fully consistent with literature data (e.g. [10–12]). The effect of intercalated stacks ($N = 2$) vs. exfoliated layers ($N = 1$) is shown to be modest for the glassy polymer nanocomposites, but more dramatic for the elastomer nanocomposites. This is also consistent with experimental data on intercalated elastomeric polyurethane/clay nanocomposites [9]. Specific comparisons between the proposed model and much of the literature data (such as [9–12]) are not possible because most authors have not provided enough detail regarding the underlying microstructure of the materials in their studies, such as L/t, silicate sheet orientation, N, $d_{(001)}$, and weight fraction. As seen in our model results, all of these factors are contributory to the end composite modulus.

The impact of multiple factors (e.g. L/t, E_p/E_m, N) on the composite modulus is emphasized by Fig. 19(d), where all model parameters are exactly those used in Fig. 19(c) except that $L = 100$ nm rather than 200 nm. The effect of L is rather dramatic, comparing Fig. 19(c) and (d). The exfoliated elastomer nanocomposite still exhibits a dramatic modulus enhancement relative to that observed in the glassy polymer nanocomposite, but the intercalated elastomer nanocomposite ($N \geq 2$) does not distinguish in as dramatic a manner from the glassy polymer nanocomposite enhancement.

6.2. Application to specific polymer–clay nanocomposite systems

6.2.1. Amorphous polymer matrix

Eastman Chemical provided injection-molded MXD6/clay nanocomposites with various clay weight fractions varying from 0 to 5.27%. The chemical structure of the polymer matrix is primarily MXD6-6007 polyamide, an amorphous polymer with high barrier properties produced by Mitsubishi Gas and Chemical Company. The layered montmorillonite clay is I.34MN organoclay from Nanocor Inc.

Material Characterization. TEM micrographs of MXD6-clay nanocomposite with various clay contents are shown in Fig. 9. Intercalated multi-layer stacks with length ~200 nm are well aligned in the flow direction. X-ray scattering reveals that the fine structure of intercalated clay stacks is independent of clay content; in particular, the average number of silicate sheets per stack is $N \sim 3$, and the average inter-layer spacing is $d_{(001)} = 4.1$ nm [40].

Experimental description. Uniaxial tensile tests are conducted on various clay content specimens with a Model-5582 Instron at room temperature and strain rate of ~0.05/s; dog-bone-shaped plate tensile specimens with gage length of 12.7 mm and thickness of 3 mm were prepared according to *ASTM D638*. For each clay content, 4–6 tests were performed. During each test, an extensometer was used to measure the axial strain; the tensile modulus of the composites was obtained from the initial slope of true stress–strain curves.

Simulation. Two-dimensional RVEs with perfect particle alignment and random particle locations were used to model the nanocomposites. Key effective particle parameters determined from Eqs. (8), (14) and (19), using $L = 200$ nm[6], $d_{(001)} = 4.1$ nm, $d_s = 0.615$ nm, $N = 3$, are the following: $L/t = 23$, $f_p/W_c = 1.20$, and $E_p/E_m = 21$. We compare the experimental data with both simulation results and predictions from the Halpin–Tsai and Mori–Tanaka models. Predicted results for the overall composite modulus are depicted in Fig. 20. Results of Mori–Tanaka model and FE simulation using the 'effective particle' concept are in good agreement with the experimental data, while the Halpin–Tsai model is too stiff. The FE models give more precise predictions than the Mori–Tanaka model, but the latter provides a reasonably accurate analytical estimate for the nanocomposite modulus.

6.2.2. Semi-crystalline polymer matrix

In semi-crystalline polymer–clay nanocomposite systems, the crystallization behavior of the matrix can be directly influenced by the presence of nanoclay particles. Both TEM and X-ray studies [34,35] of injection-molded nylon 12-clay and nylon 6-clay nanocomposites reveal that the fine lamella are oriented with their planes perpendicular to the polymer/clay interface, while the silicate sheets are aligned in the flow direction. In addition, the degree of orientation of polymer crystallites is found to increase linearly with increasing clay content, while the degree of crystallization remains constant [35]. A TEM of nylon 12-clay (Fig. 21(a), [34]) shows that this transcrystallized morphology has percolated throughout the entire matrix at a clay content of $W_c = 2\%$. Based on the above observations, it is necessary to include in the FEM simulation a third 'phase' (in addition to the effective particle and isotropic matrix) extending from the particle/polymer interfaces in order to model the transcrystallized matrix. Fig. 21(b) shows a schematic where each particle has a transcrystalline matrix layer of thickness h_{tc} on either side of it. In the following FEM calculations in this section, we assume $h_{tc} = 50$ nm[7].

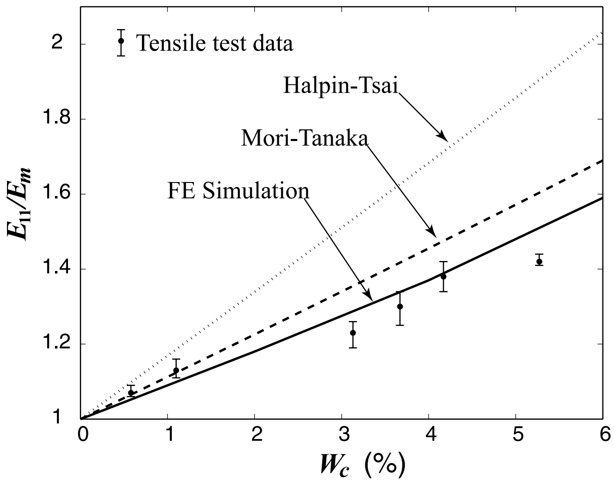

Fig. 20. Predictions of the effective longitudinal modulus for MXD6/clay nanocomposites ($L/t = 23$, $E_p/E_m = 21$, $f_p/W_c = 1.20$, $N = 3$, $d_s = 0.615$ nm, $d_{(001)} = 4.1$ nm).

Constitutive behavior of the transcrystalline matrix layer. Lin and Argon [46] produced a highly textured nylon 6 that macroscopically mimics a single crystal with orthotropic symmetry and obtained a complete set of nine elastic constants. Tzika, Boyce and Parks [47] (refer to Ref. [48] for details) used these results as guidance in determining the elastic constants and anisotropic yield surface of transcrystallized nylon 6 induced by inclusion of rubber particles; the transcrystalline material was modeled as transversely isotropic with the plane of isotropy parallel to the polymer/particle interface (plane 13 in Fig. 21(b)). Table 6 summarizes the five elastic constants with respect to the Young's modulus of the isotropic bulk matrix material (see Fig. 21(b) for coordinates). Here, we too, model the transcrystalline matrix layer with transverse isotropy, and estimate the anisotropy by using the ratios given in Table 6. Note that while E_{11} now exceeds E_m by ~30%, G_{12} is substantially lowered, which potentially compromises the load transfer efficiency from the matrix to the particle.

---

[6] Lateral dimension of montmorillonite can vary from ~100 to ~200 nm. For I.34MN organoclay, $L \sim 200$ nm.

[7] Kojima has observed that the degree of crystallite orientation increases linearly till $f_p = 0.008$ (which corresponds to $W_c = 2\%$, given $L = 100$ nm, $t = 1$ nm); together with Fig. 21(a), it is not unreasonable to assume that $W_c = 2\%$ is a critical point above which transcrystallization percolates. The inter-layer spacing for a perfectly aligned exfoliated system with $W_c = 2\%$, $L/t = 100/1$ is calculated to be ~100 nm, hence the thickness of the transcrystalline layer h_{tc} is determined as 100 nm/2 = 50 nm.

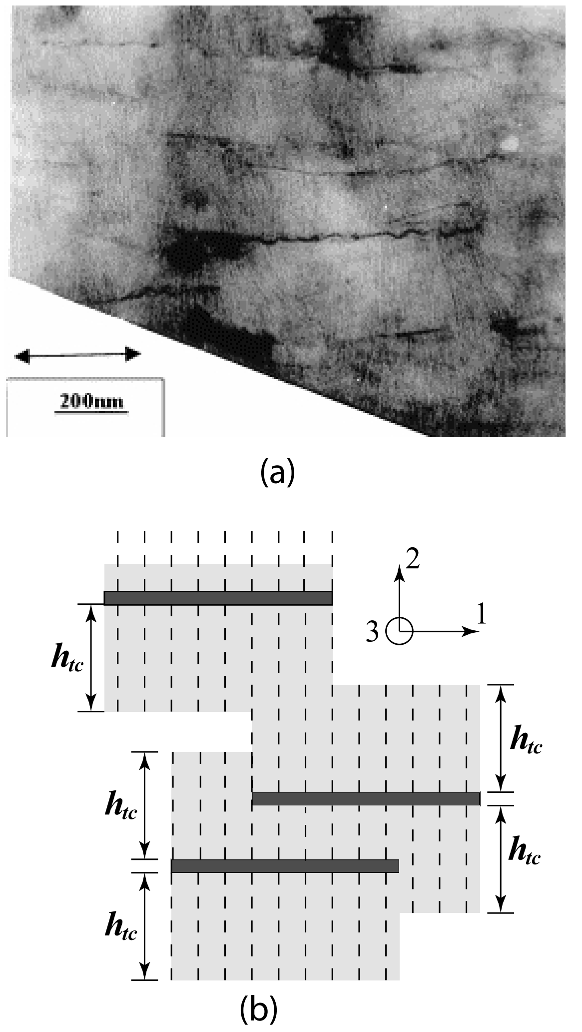

Fig. 21. (a) TEM of nylon-12/clay nanocomposite, showing a lamellar structure perpendicular to the aligned clay particles [34]. (b) Schemetic of transcrystalline matrix layers of thickness h_{tc} on both sides of the particles. The white matrix material exterior to the transcrystalline matrix layers is assumed to have isotropic elastic properties.

With the morphology and constitutive behavior of the transcrystalline matrix layer described above, we now simulate semi-crystalline polymer/clay nanocomposite systems with three phases: particle, transcrystallized anisotropic matrix, and isotropic matrix, and compare the predicted overall composite modulus with the results of experiments on nylon 6-clay nanocomposites carried out by two groups of researchers.

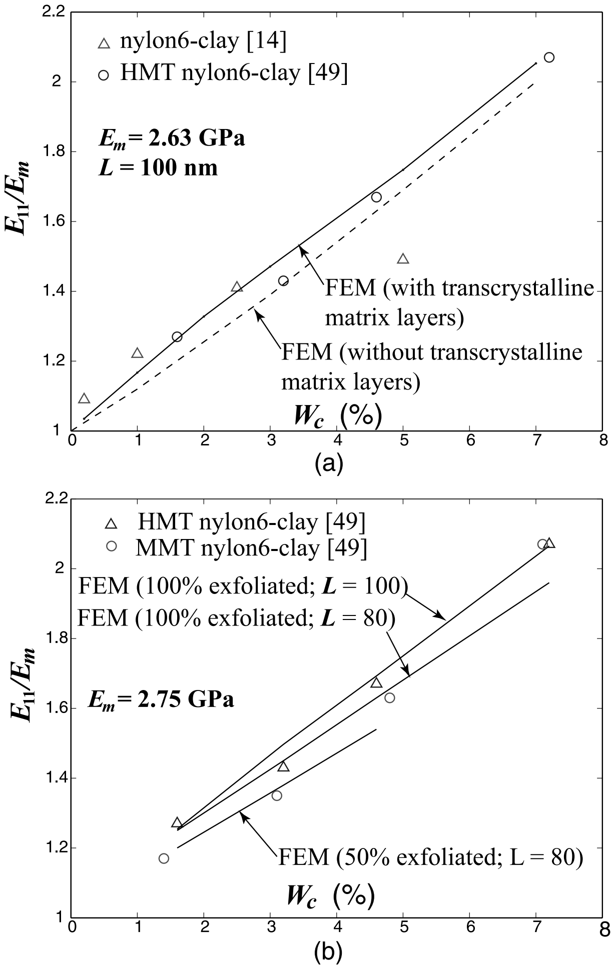

Fig. 22. (a) FEM results in comparison with experimental data for exfoliated nylon 6-clay nanocomposites at room temperature ([14], [49]). (b) FEM results (modeled with transcrystalline matrix layers) in comparison with experimental data for HMT (high molecular weight) and MMT (medium molecular weight) nylon 6-clay nanocomposites [49], where the HMT composite is completely exfoliated and the MMT composite is partially exfoliated.

Room temperature modulus of exfoliated nylon 6-clay nanocomposites with clay contents varying from 0.2 to 7.2 wt% are obtained from van Es et al.[8] [14] and Fornes et al. [49]. Both groups claim nearly complete exfoliation and good particle alignment for partial (up to 5 wt% for van Es et al.) or complete range of the clay content. RVEs with well-aligned particles ($L/t = 100/1^9$) are generated to model the fully exfoliated systems. FEM results with and without transcrystalline matrix layers are plotted, together with experimental data, in Fig. 22(a). The elastic constants of the transcrystalline material are calculated from the matrix

Table 6
Elastic constants of transcrystalline nylon 6, normalized with E_{m}, Young's modulus of isotropic matrix [47]

$E_{11,\text{tc}}/E_{\text{m}}$	$E_{22,\text{tc}}/E_{\text{m}}$	$\nu_{12,\text{tc}}$	$\nu_{13,\text{tc}}$	$G_{12,\text{tc}}/E_{\text{m}}$
1.29	0.99	0.53	0.33	0.11

Refer to Fig. 21(b) for coordinates.

---

[8] van Es et al. performed DMTA tests and extracted storage modulus from the DMTA data at fixed temperatures. Here, we analyze their data at $T = 23$ °C.

[9] Here, we assume the thickness of a single silicate layer, d_{s}, to be 1 nm, as is often referred to in related literature. The corresponding silicate stiffness is $E_{\text{silicate}} = 250$ GPa; however, the specific values of the pair (d_{s}, E_{silicate}) have little effect on the predicted macroscopic composite modulus.

modulus at 0% clay concentration, E_m, and the ratios given in Table 6 (E_m is given as 2.63 and 2.75 GPa from Ref. [14] and [49], respectively; we use the former value as there is no need for distinction).

The models with added transcrystalline matrix layers give results in excellent agreement with experimental data; however the DMTA data from van Es et al. severely levels off at $W_c = 5\%$, which is suspected to have resulted from poor particle alignment and/or imperfect exfoliation.[10] While the transcrystallization of the matrix does contribute to the enhancement of the overall composite modulus, the dominant reinforcing source is still the clay particles (at $W_c = 7\%$, the perfectly aligned clay increased the composite modulus by $\sim 100\%$, whereas the presence of transcrystalline layers added only an additional 5%). One should also bear in mind that although $E_{11,tc}$ is about 30% higher than E_m (Table 6), the low $G_{12,tc}$ tends to lower the efficiency of load transfer from the matrix to the particles, which explains why at $W_c = 7\%$, when the transcrystalline structure has percolated, the predicted additional modulus increase from the special matrix morphology is 5% rather than 30%. It's also interesting to notice that a slight decrease in slope occurs at $\sim W_c = 2\%$, which is consistent with our assumption that 2 wt% is the critical exfoliated clay content above which matrix transcrystallization percolates.

Another important aspect to explore is the effect of imperfect exfoliation. Fornes and coworkers [49] studied the dependency of composite tensile modulus on matrix molecular weight, which essentially affects the degree of exfoliation; in particular, their low molecular weight nylon 6-clay system is intercalated, their medium molecular weight (MMT) system is partially exfoliated, and their high molecular weight (HMT) system is nearly completely exfoliated. We simulate the MMT and HMT composite systems in order to verify the model capability to capture the effects of imperfect exfoliation as well as the effect of particle-induced transcrystallization of the matrix. TEM micrographs reveal that while the HMT composite is dominated by individual silicate layers with the presence of a few intercalated stacks (the averaged number of layers per stack $\bar{N} \sim 1.3$), the MMT system contains a higher fraction of multi-layer stacks ($\bar{N} \sim 1.5$).

To simulate the HMT composite, we generated RVEs containing particles of uniform length and thickness (the small fraction of intercalated stacks are neglected); two particle lengths are used in the FEM calculations: $L = 80$ nm and $L = 100$ nm, the former value reported by Fornes et al. [49], based on TEM micrographs, and the latter value usually cited in the literature for a typical length of montmorillonite. To simulate the MMT composite, we generated RVEs containing particles with a distribution in thickness, mimicking a system with 50% of silicate mass in two-layer stacks and the remaining 50% in exfoliated layers.[11] Transcrystalline matrix layers with thickness of $h_{tc} = 50$ nm are included in all of the simulations. FEM results for E_{11}/E_m as a function of W_c for the above composite systems are plotted in Fig. 22(b), together with the HMT and MMT experimental data. Composite moduli of both exfoliated and partially exfoliated systems, predicted by the modified model, are in good agreement with experimental data. The presence of intercalated stacks clearly impairs the stiffness reinforcing efficiency of a nearly exfoliated system—these stacks not only have lower modulus compared with a silicate sheet, they also provide less external interface areas for induction of transcrystalline matrix material (since some silicate layer surfaces are now inside a particle instead of dispersed in the matrix).

6.3. *Effect of melt-processing towards complete exfoliation*

Melt-processing has been observed to have an impact on the morphology of polymer/clay nanocomposites. Delamination (a decrease in N) and inter-layer swelling (an increase in $d_{(001)}$) result from melt-processing, as reported in Ref. [50,51]. As an example, we study the effect of melt-processing on MXD6/clay nanocomposite taken from Lee and McKinley [40]. The amorphous MXD6 matrix reduces the complexity of the nanocomposite system, allowing us to focus on the effect of morphological changes in the particle phase only.

Injection-molded MXD6/clay nanocomposite ($W_c = 5.27\%$) after melt-processing (screw RPM = 150, $T = 250$ °C) exhibit structure changes in the nanoclay [40]. The as-received material has an intercalated morphology; after processing, the average value of N decreases from ~ 3 to ~ 2, and the average inter-layer spacing, $d_{(001)}$, increases from **4.1** to **4.5** nm. In the limiting case of complete exfoliation, $N \rightarrow 1$.

As the clay internal structure evolves towards smaller N and larger $d_{(001)}$, ultimately reaching $N = 1$, substantial changes in the effective 'particle' properties occur: particle aspect ratio increases (Eq. (8)), particle stiffness also increases (Fig. 15); however, for a fixed W_c, particle volume fraction decreases (Fig. 13). These evolving effective 'particle' properties accompanying evolving clay structure, caused by processing towards exfoliation, are listed in Table 7. Note that when N decreases from 2 to 1, there is a dramatic increase in both L/t and E_p/E_m, but also a corresponding abrupt drop in f_p/W_c.

FEM calculations of the overall plane strain composite modulus, E_{11}/E_m, for material as received, after processing,

---

[10] For a fully percolated system ($W_c > 2\%$), given perfect particle alignment, the transcrystalline material alone increases the modulus by 30% ($E_{11,tc}/E_m \sim 1.3$). Thus, the fact that the composite modulus (DMTA data) only increased by $\sim 40\%$ at $W_c = 5\%$ indicates a substantial degree of particle misalignment.

[11] Suppose we have a total number of 100 silicate sheets. 50% two-layer stacks gives 25 ($100 \times 50\%/2 = 25$) particles with a thickness of $d_{(001)} + d_s$, while the remaining 50 sheets are particles with a thickness of d_s. In our simulation, it is assumed that $d_{(001)} = 4$ nm, and $d_s = 1$ nm.

Table 7
Evolution of the effective particle's structure and properties as intercalated structure is processed towards exfoliation

Material	N	$d_{(001)}$ (nm)	χ	L/t	f_p/W_c	E_p/E_m
MXD 6/clay (as-received)	~3	4.1	0.21	23	1.20	21
After processing	~2	4.5	0.24	39	1.04	24
Completely exfoliated	1		1.0	325	0.25	100

Resulting macroscopic stiffness shown in Fig. 23. $L = 200$ nm, $d_s = 0.615$ nm.

and completely exfoliated (model parameters given in Table 7), are depicted in Fig. 23. The modulus increase associated with increasing degree of exfoliation can be attributed to the increased particle aspect ratio and particle stiffness. Note that the extremely large L/t and E_p/E_m when $N = 1$ did not bring about a dramatic jump in E_{11} due to the significantly reduced effective particle volume fraction for a fixed clay weight fraction, and to strong particle interference in load transfer efficiency. It should also be noted that the particles are assumed to remain planar in the modeling. However, TEM images show that fully exfoliated single silicate layers and two-layer particles have a greater tendency to be curved, compared to particles with more layers; this increased bending compliance and resulting angular misorientation will further reduce the efficiency of fully exfoliated particles in enhancing the composite modulus. Thus, considering processing difficulties, complete exfoliation may not be the optimal choice as far as the overall stiffness is concerned, unless exfoliated particle bending and misorientation can be effectively suppressed.

7. Conclusions

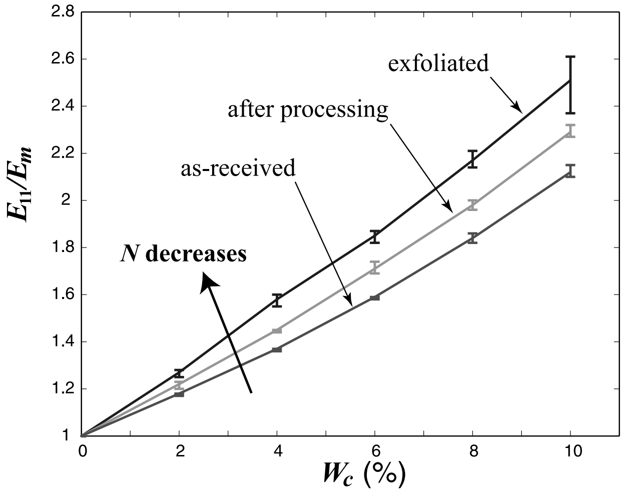

Fig. 23. Effect of processing towards complete exfoliation on the overall composite stiffness. Each FEM data point is averaged over results of 10 random RVE realizations; variation is reflected by error bars.

Continuum-based micromechanical models can provide robust predictions of the overall elastic properties of polymer/clay nanocomposites, provided that a reliable method is employed to account for the intrinsically hierarchical morphology of intercalated nanoclay, and for the special matrix morphology and properties adjacent to the particles. The intercalated nanoclay, idealized as a multi-layer stack with N silicate sheets and inter-layer spacing of $d_{(001)}$, can be effectively represented as a homogeneous 'particle', which possesses the same spatial domain occupied by both the silicate layers and the inter-layer galleries. Transcrystallization behavior in semi-crystalline polymer matrix, induced by the presence of nanoclay, is taken into account by adding highly anisotropic matrix layers around the particles. A careful mapping between the characteristic clay structural parameters (N, $d_{(001)}$) and clay weight fraction (W_c) and the conventional micromechanical model parameters (particle volume fraction f_p, particle aspect ratio L/t, and particle elastic behavior) is established. Various two-dimensional RVEs of the underlying structure of polymer/clay nanocomposite are constructed. In nanocomposites with aligned particles, the almost negligible difference in the predicted overall axial modulus whether the clay is constitutively modeled as a 'discrete stack' or a homogenized 'effective particle', adds additional justification to the multi-scale modeling strategy. In the presence of nonaxial loading or particle misalignment, the orthotropic rather than isotropic 'effective particle' should be used in order to account for the potentially low shear modulus of the inter-layer galleries. The model is found to capture the strong enhancement in composite modulus observed for elastomer/nanoclay nanocomposites as compared with the more moderate enhancements observed in glassy and semicrystalline thermoplastics as well as epoxies. The model prediction of the overall modulus of well-characterized amorphous (MXD6) and semi-crystalline (nylon 6) polymer–clay nanocomposites are in good agreement with experimental data. This scheme is also used to predict the ultimate stiffness that can be achieved in the nanocomposite by processing towards complete exfoliation. In contrast to expectation, there is no abrupt stiffness increase associated with morphological transition from intercalation ($N \geq 2$) to exfoliation ($N = 1$) when examining the effect of clay weight fraction on macroscopic stiffness.

Acknowledgements

This research was funded through the Air Force sponsored DURINT project on Polymer Nanocomposites under grant number F49620-01-1-0447. We acknowledge discussions with our collaborators G. H. McKinley and H. Lee. We also acknowledge interactions with J. Gilmer of Eastman Chemical and, in particular, the generous processing and supply of materials.

References

[1] Shepherd PD, Golemba FJ, Maine FW. Adv Chem Ser 1974;134:41.
[2] Usuki A, Kojima Y, Kawasumi M, Okada A, Fukushima Y, Kurauchi T, Kamigaito O. J Mater Res 1993;8:1179.
[3] Kojima Y, Usuki A, Kawasumi M, Okada A, Fukushima Y, Kurauchi T, Kamigaito O. J Mater Res 1993;8:1185.
[4] Yano K, Usuki A, Okada A, Kurauchi T, Kamigaito O. J Polym Sci, Polym Chem 1993;31:2493.
[5] Messersmith PB, Giannelis EP. Chem Mater 1994;6:1719.
[6] Messersmith PB, Giannelis EP. J Polym Sci, Polym Chem 1995;33:1047.
[7] Gilman JW. Appl Clay Sci 1999;15:31.
[8] Vaia RA, Price G, Ruth PN, Nguyen HT, Lichtenhan J. Appl Clay Sci 1999;15:67.
[9] Wang Z, Pinnavaia TJ. Chem Mater 1998;10:3769.
[10] Burnside SD, Giannelis EP. J Polym Sci, Polym Phys 2000;38:1595.
[11] Triantafillidis CS, LeBaron PC, Pinnavaia TJ. J Solid State Chem 2002;167:354.
[12] Ratna D, Manoj NR, Varley R, Singh Raman RK, Simon GP. Polym Int 2003;52:1403.
[13] Nam PH, Maiti P, Okamoto M, Kotaka T, Hasegawa N, Usuki A. Polymer 2001;42:9633.
[14] van Es M, Xiqiao F, van Turnhout J, van der Giessen E. In: Al-Malaika S, Golovoy A, Wikie CA, editors. Specialty polymer additives. Malden, MA: Blackwell Science; 2001.
[15] Brune DA, Bicerano J. Polymer 2002;43:369.
[16] Yoon PJ, Fornes TD, Paul DR. Polymer 2002;43:6727.
[17] Eshelby JD. Proc R Soc A 1957;241:376.
[18] Hill R. J Mech Phys Solids 1965;13:213.
[19] Hermans J. J Proc Kon Ned Akad v Wetensch B 1967;65:1.
[20] Mori T, Tanaka K. Acta Metall Mater 1973;21:571.
[21] Ashton JE, Halpin JC, Petit PH. Primer on composite materials: analysis. Stamford Conn: Technomic; 1969.
[22] Halpin JC. J Compos Mater 1969;3:732.
[23] Halpin JC, Kardos JL. Polym Engng Sci 1976;16:344.
[24] Cox HL. Br J Appl Phys 1952;3:72.
[25] Hill R. Proc Phys Soc A 1952;65:349.
[26] Tucker CL, Liang E. Compos Sci Technol 1999;59:655.
[27] Tandon GP, Weng GJ. Polym Compos 1984;5:327.
[28] Bergström JS, Boyce MC. Rubber Chem Technol 1999;72:633.
[29] Gusev AA. Macromolecules 2001;34:3081.
[30] Danielsson M, Parks DM, Boyce MC. J Mech Phys Solids 2002;50:351.
[31] Loo LS, Gleason KK. Macromolecules 2003;36:2587.
[32] Brown JM, Curliss D, Vaia RA. Chem Mater 2000;12:3376.
[33] Vaia RA. In: Pinniavaia TJ, Beall GW, editors. Polymer clay nanocomposites. New York: Wiley; 2000.
[34] Kim GM, Lee DH, Hoffmann B, Kressler J, Stoppelmann G. Polymer 2001;42:1095.
[35] Kojima Y, Usuki A, Kawasumi M, Okada A, Kurauchi T, Kamigaito O, Kaji K. J Polym Sci, Polym Phys 1994;32:625.
[36] Chacko VP, Karasz FE, Farris RJ, Thomas EL. J Polym Sci, Polym Phys 1982;20:2177.
[37] Bartczak Z, Argon AS, Cohen RE, Kowalewski T. Polymer 1999;40:2367.
[38] Muratoglu OK, Argon OS, Cohen RE. Polymer 1995;36:2143.
[39] Muratoglu OK, Argon OS, Cohen RE. Polymer 1995;36:921.
[40] Lee H, Cohen RE, McKinley GH. Manuscript in preparation.
[41] Yakobson BI, Brabec CJ, Bernholc J. Phys Rev Lett 1996;76:2511.
[42] Pantano A, Parks DM, Boyce MC. J Mech Phys Solids 2003; in press.
[43] Manevitch OL, Rutledge GC. Elastic properties of a single lamella of montmorillonite by molecular dynamics simulation. J Phys Chem B 2003; In press.
[44] Yasue K, Katahira S, Yoshikawa M, Fujimoto K. In: Pinniavaia TJ, Beall GW, editors. Polymer clay nanocomposites. New York: Wiley; 2000.
[45] Beall GW. In: Pinniavaia TJ, Beall GW, editors. Polymer clay nanocomposites. New York: Wiley; 2000.
[46] Lin L, Argon AS. Macromolecules 1992;25:4011.
[47] Tzika PA, Boyce MC, Parks DM. J Mech Phys Solids 2000;48:1893.
[48] Tzika PA. Micromechanical modeling of the toughening mechanisms in particle-modified semicrystalline polymers, Thesis (S.M.), Massachusetts Institute of Technology, Department of Mechanical Engineering, 1999.
[49] Fornes TD, Yoon PJ, Keskkula H, Paul DR. Polymer 2001;42:9929.
[50] Dennis HR, Hunter DL, Chang D, Kim S, White JL, Cho JW, Paul DR. Polymer 2001;42:9513.
[51] Liu LM, Qi ZN, Zhu XG. J Appl Polym Sci 1999;71:1133.